Speed Sensorless Nonlinear Adaptive Control of Induction Motor using Combined Speed and Perturbation Observer

Yaxing Ren[a,b], Ruotong Wang[b,c], Saqib Jamshed Rind[b,d], Pingliang Zeng[a], Lin Jiang[b,**]

[a]*Hangzhou Dianzi University, Xiasha, Hangzhou, 310018, China*
[b]*Department of Electrical & Electronics Engineering, University of Liverpool, Liverpool, L69 3BX, UK*
[c]*Shandong Artificial Intelligence Institute, Qilu University of Technology (Shandong Academy of Sciences), Jinan, 250316, China*
[d]*Department of Automotive and Marine Engineering, NED University of Engineering and Technology, Karachi, 75270, Pakistan*

Abstract

High performance induction motors (IM) require a robust and reliable speed controller to maintain the speed tracking performance under various uncertainties and disturbances. This paper presents a sensorless speed controller for IM based on speed and perturbation estimation and compensation. By defining a lumped perturbation term to include all unmodeled nonlinear dynamics and external disturbances, two state and perturbation observers are designed with combining the model reference adaptive system (MRAS) based speed observer to estimate the flux and speed states and the flux- and speed-loop related lumped perturbation terms. The estimated flux, speed

*This work was funded by '2018 Huzhou South Taihu Elite Program Leading Innovation Team Project'.

**Corresponding author.
Email address: L.Jiang@liv.ac.uk (Lin Jiang)

and perturbation terms are used to design an output feedback, speed sensorless nonlinear adaptive controller (SSNAC) for IM. The stability of the closed-loop system is addressed in Lyapunov theory. Effectiveness of the SSNAC is verified via simulation and experiment tests. Comparing with the standard vector control plus MRAS speed observer (VC-MRAS), the proposed SSNAC reduces the speed tracking error by 20% to 30% on average under model uncertainties and unknown load disturbance due to the estimation and compensation of perturbation terms. The combined observer can estimate the real rotor speed under speed varying and load changes and thus makes SSNAC achieve high performance robust speed drive without using speed sensors.
Keywords: Perturbation estimation and compensation, nonlinear adaptive control, speed sensorless control, combined speed and perturbation observer, induction motor

1. Introduction

Induction motors (IM) have been widely used as the main power force in industry such as various household products and industrial applications, and also for the developed electric vehicle such as Tesla, due to their simplistic construction and reliable performance in harsh environment (Hu et al. (2014)). However, control of IM is a challenge task due to its highly coupled nonlinear nature, the unmeasurable rotor side variables and flux linkage and uncertainties from the parameters and the load (Finch and Giaouris (2008)). At present, the most widely applied control approaches for IM are the vector control (VC) and direct torque control (DTC) (Rehman and Xu (2011)). The

DTC is a lookup table based control approach that directly adjusts the stator voltage using space vector technology to avoid the complex coordination transformation on stator current and therefore results in a rapid response of torque (Rind et al. (2017); Costa et al. (2019)). The VC, also called field-oriented control, can successively regulate the magnetic flux amplitude and the rotor mechanical speed to track their references (Bhowate et al. (2019)). However, the traditional VC method can only realize the asymptotic input-output linearisation of the IM system and cannot fully linearise the nonlinear dynamic of the IM system and the neglected nonlinear coupling can seriously affect the dynamics of the magnetic flux loop and the speed loop under external disturbances (Marino et al. (1993); Liu et al. (2013)).

IM traction drives require high-performance controllers for fast transient response as well as energy optimisation. One of the most used control methods for nonlinear systems is the input-output linearisation control (IOLC) to achieve complete decoupling of rotor speed and flux linkage. This method can simultaneously adjust the speed and magnetic flux without ignoring the coupling nonlinear dynamics between them. Based on this method, some approaches for IM speed drive have been proposed, such as the adaptive input-output linearisation control (Marino et al. (1993)), nonlinear precision feedback linearisation control (Boukas and Habetler (2004)) that can fully linearise the flux linkage and speed to decouple their dynamics, and nonlinear model predictive control to solve the optimal control problem (Englert and Graichen (2020)). The main drawback of IOLC method is that it requires detailed system models and accurate model parameters. In practical applications, the system parameters are difficult to obtain accurately, such as the

time-varying rotor/stator resistance (Guzinski and Abu-Rub (2013)). In this way, the robustness and reliability of the IOLC method are greatly reduced. In response to this problem, researchers have developed disturbance estimation and compensation methods based nonlinear adaptive control (Jiang et al. (2004); Chen et al. (2019b,a)). These methods use online estimation and compensation the lumped perturbation term that including the nonlinear parts, external disturbances, and parameter changes. Thus, its performance does not depend on the accuracy of the IM model. In addition, there are online parameter estimation techniques (Proca and Keyhani (2007); Ravi Teja et al. (2012); Kivanc and Ozturk (2018); Yang et al. (2018); Pyrkin et al. (2019); Perin et al. (2021)), estimating the rotor resistance via stator temperature to compensate temperature variation (Sung et al. (2012)), sliding mode control (Wu et al. (2013); Wang et al. (2018a)), combined sliding mode techniques with MRAS-type estimator (Tarchała and Orłowska-Kowalska (2018); Holakooie et al. (2019)), fuzzy control (Suetake et al. (2011); Grabowski et al. (2000)), and auto-disturbance rejection control (Feng et al. (2004); Li et al. (2012, 2015)), etc.

On the other hand, the traditional IM speed control is based on speed feedback from encoder or position sensors. However, due to the reliability of the sensors as well as the electrical noise of the sensor itself, if the speed is only obtained from the sensors, the overall reliability of the system will be reduced, such as the impact of sensor fault (Verrelli et al. (2018)). Therefore, in addition to installing a speed encoder, it is also considered to use sensorless control that estimates the rotor speed in high-performance IM and EV applications (Holtz (2005)). Due to the rapid development of power electronics

technology and digital signal processor performance, the sensorless control method of IM becomes increasing more feasible. There have been a lot of research results on the speed estimation of sensorless control, such as estimated rotor position and velocity calculated from stationary frame (Nasiri (2007)), rotor flux observer based algorithm (Marchesoni et al. (2020)), optimization-based position sensorless control (Callegaro et al. (2018)), model reference adaptive system (MRAS) speed observer (Schauder (1992); Ohyama et al. (2005)), MRAS-fuzzy logic observer (Gadoue et al. (2010)), easy implement PLL-like sensorless observer (Tilli and Conficoni (2016)), sliding mode techniques based speed observer (Li et al. (2005); Zhang (2013); Zaky et al. (2018)), extended Kalman filter for speed estimation (Habibullah and Lu (2015)), artificial neural network speed observer (Sun et al. (2013)), and approximate high gain observer (Wang et al. (2018b)), etc. The MRAS speed observer based on rotor flux equations is the most preferable scheme due to its easy implementation and clear physical meaning (Yang et al. (2018)). Most MRAS speed observer is using the rated parameters of the IM and assuming the parameters are constant. To solve this issue, some parameter estimation approaches have been proposed to deal with unknown constant or slow-varying parameters (Marino et al. (2005, 2008); Tilli and Conficoni (2016)). But these algorithms work under the constant or slow-varying speed conditions which is not quite suitable in EV application. Moreover, the disturbance observer based control algorithm uses a state observer to estimate the lumped nonlinear terms and disturbances, while the speed observer estimates the rotor speed. Then it will raise a question that, if the disturbance observer based control algorithm is combined with the speed sensorless

method, whether the speed estimator affects the robustness and control performance of the control algorithm. Another question is whether they can be combined in some way to estimate speed and disturbance at the same time, thereby reducing the amount of calculation.

In this paper, a speed sensorless nonlinear adaptive controller (SSNAC) has been proposed to integrate the nonlinear control techniques and traditional speed estimation techniques to provide a nonlinear sensorless drive of an IM. The SSNAC is designed using the MRAS speed observer to estimate the rotor speed and two state and perturbation observers (SPO) to estimate the perturbation terms of the flux and speed loop. Moreover, a combined speed and perturbation observer (CSPO) is proposed to estimate the speed and perturbation terms simultaneously. It reduced the usage of a PI regulator in the traditional MRAS speed estimator for the reduction of computational load. The estimated perturbation term from the CSPO is used to compensate the real value of speed perturbation in order to reduce the dependency of accurate model and parameters for improved robustness of the control method. The stability of closed-loop system that integrates the nonlinear control techniques and speed estimation with a combined speed and perturbation observer is proved using Lyapunov theory.

The remainder of this paper is organised as follows. Section 2 presents the IM dynamic model in the d-q frame. Section 3 presents the design of the proposed SSNAC controller. The stability proof of the closed-loop system is presented in Section 4. The effective application of NAC is validated in simulation and presented in Section 5 and validated experimentally in Section 6. Finally, the paper concludes in Section 7.

2. Model of Induction Motor

A three-phase would-rotor IM can be transformed into rotating frame in d-q axis via Park transform with the d-axis synchronize with the angle of rotor flux θ_r. Then the dynamic model of an IM can be presented as follows (Bimal (2002)):

$$\dot{x} = f(x) + Gu \tag{1}$$

where

$$x = \begin{bmatrix} i_{\mathrm{sd}} & i_{\mathrm{sq}} & \psi_{\mathrm{rd}} & \psi_{\mathrm{rq}} & \omega_{\mathrm{m}} \end{bmatrix}^T$$

$$f(x) = \begin{bmatrix} -\left(\dfrac{R_{\mathrm{s}}}{\sigma L_{\mathrm{s}}} + \dfrac{R_{\mathrm{r}} L_{\mathrm{m}}^2}{\sigma L_{\mathrm{s}} L_{\mathrm{r}}^2}\right) i_{\mathrm{sd}} + \omega_{\mathrm{e}} i_{\mathrm{sq}} + \dfrac{R_{\mathrm{r}} L_{\mathrm{m}}}{\sigma L_{\mathrm{s}} L_{\mathrm{r}}^2} \psi_{\mathrm{rd}} + \dfrac{\omega_{\mathrm{r}} L_{\mathrm{m}}}{\sigma L_{\mathrm{s}} L_{\mathrm{r}}} \psi_{\mathrm{rq}} \\ -\left(\dfrac{R_{\mathrm{s}}}{\sigma L_{\mathrm{s}}} + \dfrac{R_{\mathrm{r}} L_{\mathrm{m}}^2}{\sigma L_{\mathrm{s}} L_{\mathrm{r}}^2}\right) i_{\mathrm{sq}} - \omega_{\mathrm{e}} i_{\mathrm{sd}} - \dfrac{\omega_{\mathrm{r}} L_{\mathrm{m}}}{\sigma L_{\mathrm{s}} L_{\mathrm{r}}} \psi_{\mathrm{rd}} + \dfrac{R_{\mathrm{r}} L_{\mathrm{m}}}{\sigma L_{\mathrm{s}} L_{\mathrm{r}}^2} \psi_{\mathrm{rq}} \\ -\dfrac{R_{\mathrm{r}}}{L_{\mathrm{r}}} \psi_{\mathrm{rd}} + (\omega_{\mathrm{e}} - \omega_{\mathrm{r}}) \psi_{\mathrm{rq}} + \dfrac{R_{\mathrm{r}} L_{\mathrm{m}}}{L_{\mathrm{r}}} i_{\mathrm{sd}} \\ -\dfrac{R_{\mathrm{r}}}{L_{\mathrm{r}}} \psi_{\mathrm{rq}} - (\omega_{\mathrm{e}} - \omega_{\mathrm{r}}) \psi_{\mathrm{rd}} + \dfrac{R_{\mathrm{r}} L_{\mathrm{m}}}{L_{\mathrm{r}}} i_{\mathrm{sq}} \\ \dfrac{3PL_{\mathrm{m}}}{2JL_{\mathrm{r}}} \left(\psi_{\mathrm{rd}} i_{\mathrm{sq}} - \psi_{\mathrm{rq}} i_{\mathrm{sd}}\right) - \dfrac{T_{\mathrm{L}}}{J} \end{bmatrix}$$

$$G = \begin{bmatrix} \dfrac{1}{\sigma L_{\mathrm{s}}} & 0 & 0 & 0 & 0 \\ 0 & \dfrac{1}{\sigma L_{\mathrm{s}}} & 0 & 0 & 0 \end{bmatrix}^T$$

$$u = \begin{bmatrix} u_1 & u_2 \end{bmatrix}^T = \begin{bmatrix} v_{\mathrm{sd}} & v_{\mathrm{sq}} \end{bmatrix}^T$$

where x is the states vector of IM system with five state variables, i_{sd} and i_{sq} are the stator current in d-q frame, ψ_{rd} and ψ_{rq} are the rotor flux linkage,

ω_{m} is the mechanical rotor speed. $f(x)$ is the nonlinear function of state dynamics. R_{s}, R_{r}, L_{s} and L_{r} are the resistances and inductances of stator and rotor; L_{m} is the mutual inductance between stator and rotor phase winding; $\sigma = 1 - L_{\mathrm{m}}^2/L_{\mathrm{s}}L_{\mathrm{r}}$ is the parameter that indicates the leakage factor. ω_{e} is the synchronous speed of stator current; ω_{r} is the rotor speed in electrical that satisfies $\omega_{\mathrm{r}} = P\omega_{\mathrm{m}}$, P is the pole pairs of IM. J is the rotor inertia and T_{L} is the load torque which is seen as a disturbance. G is the matrix gain of system inputs. u is the control inputs of IM system with two input variables, v_{sd} and v_{sq}, the stator voltage inputs. The system output is defined in a vector y, which is presented as

$$y = \begin{bmatrix} |\psi_{\mathrm{r}}| & \omega_{\mathrm{m}} \end{bmatrix}^T \tag{2}$$

where

$$|\psi_{\mathrm{r}}| = \sqrt{\psi_{\mathrm{rd}}^2 + \psi_{\mathrm{rq}}^2} \tag{3}$$

and the rotor currents i_{rd} and i_{rq} can be expressed as

$$\begin{cases} i_{\mathrm{rd}} = \dfrac{1}{L_{\mathrm{s}}}\psi_{\mathrm{rd}} - \dfrac{L_{\mathrm{m}}}{L_{\mathrm{r}}}i_{\mathrm{sd}} \\ i_{\mathrm{rq}} = \dfrac{1}{L_{\mathrm{s}}}\psi_{\mathrm{rq}} - \dfrac{L_{\mathrm{m}}}{L_{\mathrm{r}}}i_{\mathrm{sq}} \end{cases} \tag{4}$$

3. Speed sensorless nonlinear adaptive controller

This section introduces the design steps of the perturbation observer based nonlinear adaptive controller (NAC) and combines it with the rotor-flux based MRAS speed observer to become a speed sensorless control system for IM. The NAC design uses the input-output linearisation to fully decouple the interaction between the flux linkage and speed subsystems. Then

the system nonlinearities, disturbances, and parameter uncertainties are defined as perturbation terms (Ren et al. (2016)). After that, two state and perturbation observers (SPOs), one for the flux linkage loop and the other for the speed loop, are designed to estimate their perturbation terms. The speed sensorless feedback controller is fed by the speed estimation from the MRAS speed observer, which uses a PI regulator to eliminate the estimation error. Moreover, the speed SPO and MRAS speed observer are combined to a speed and perturbation observer that is able to estimate both the rotor speed and its perturbation term simultaneously and the usage of PI regulator in traditional MRAS is then removed.

3.1. Input-output linearisation

In the $d-q$ frame dynamic model of IM in (1), the d-axis is aligned with the direction of rotor flux. Then it can be assumed that $\psi_{\mathrm{rd}} = \psi_{\mathrm{r}}$, and $\psi_{\mathrm{rq}} = 0$ in steady state (Bimal (2002)).

Differentiate the system output y until the system inputs is separated with other states, the input-output relationship of the IM system is obtained as Chen et al. (2014):

$$\begin{bmatrix} \ddot{y}_1 \\ \ddot{y}_2 \end{bmatrix} = \begin{bmatrix} L_{f1}(x) \\ L_{f2}(x) \end{bmatrix} + B(x) \begin{bmatrix} u_1 \\ u_2 \end{bmatrix} \tag{5}$$

$$L_{f1}(x) = \frac{R_{\mathrm{r}}^2}{\sigma L_{\mathrm{r}}^2}\psi_{\mathrm{r}}(x) - \frac{L_{\mathrm{m}}R_{\mathrm{r}}}{\sigma L_{\mathrm{r}}}\left(\frac{R_{\mathrm{r}}}{L_{\mathrm{r}}} + \frac{R_{\mathrm{s}}}{L_{\mathrm{s}}}\right) i_{\mathrm{sd}}(x) + \frac{L_{\mathrm{m}}R_{\mathrm{r}}}{L_{\mathrm{r}}}\omega_{\mathrm{e}} i_{\mathrm{sq}}(x) \tag{6}$$

$$\begin{aligned} L_{f2}(x) = \frac{3PL_{\mathrm{m}}}{2JL_{\mathrm{r}}}\Bigg[& -\left(\frac{R_{\mathrm{s}}}{\sigma L_{\mathrm{s}}} + \frac{R_{\mathrm{r}}}{\sigma L_{\mathrm{r}}}\right)\psi_{\mathrm{r}}(x) i_{\mathrm{sq}}(x) - \omega_{\mathrm{e}}\psi_{\mathrm{r}}(x) i_{\mathrm{sd}}(x) \\ & + \frac{L_{\mathrm{m}}R_{\mathrm{r}}}{L_{\mathrm{r}}} i_{\mathrm{sd}}(x) i_{\mathrm{sq}}(x) - \frac{L_{\mathrm{m}}}{\sigma L_{\mathrm{s}}L_{\mathrm{r}}}\omega_{\mathrm{r}}(x)\psi_{\mathrm{r}}(x)^2 \Bigg] - \frac{1}{J}\dot{T}_{\mathrm{L}}(x) \end{aligned} \tag{7}$$

$$B(x) = \begin{bmatrix} B_1(x) \\ B_2(x) \end{bmatrix} = \begin{bmatrix} \frac{L_{\mathrm{m}} R_{\mathrm{r}}}{\sigma L_{\mathrm{s}} L_{\mathrm{r}}} & 0 \\ 0 & \frac{3PL_{\mathrm{m}}\psi_{\mathrm{r}}(x)}{2J\sigma L_{\mathrm{s}} L_{\mathrm{r}}} \end{bmatrix} \tag{8}$$

where $L_{f1}(x)$ and $L_{f2}(x)$ represent the system nonlinearities which are function of system states and parameters. As during the normal operation $\psi_{\mathrm{r}} \neq 0$, $|B(x)| \neq 0$ and $B(x)$ is a non-singular matrix, thus the feedback linearising control can be obtained as

$$\begin{bmatrix} u_1 \\ u_2 \end{bmatrix} = B^{-1}(x) \left(\begin{bmatrix} -L_{f1}(x) \\ -L_{f2}(x) \end{bmatrix} + \begin{bmatrix} \upsilon_1 \\ \upsilon_2 \end{bmatrix} \right), \tag{9}$$

where υ_1 and υ_2 are the control inputs of the linear system

$$\begin{bmatrix} \ddot{y}_1 \\ \ddot{y}_2 \end{bmatrix} = \begin{bmatrix} \upsilon_1 \\ \upsilon_2 \end{bmatrix}. \tag{10}$$

3.2. Design of state and perturbation observer design

The first step of design the state and perturbation observer (SPO) is to define the perturbation terms. The value of $B(x)$ is time varying due to the changes of states and parameter uncertainties, such as J and τ_r. Define $B(x) = B_0 + \Delta B$, B_0 is the nominal value of $B(x)$ and calculated by using the nominal value of rotor flux ψ_{r0} and all parameters, and ΔB represents uncertainties of the control gain matrix caused from the parameter uncertainties and operation point changes. For example, the rotor resistance can be described as the rated resistance plus the varying of rotor resistance as $R_{\mathrm{r}} = R_{\mathrm{r0}} + \Delta R_{\mathrm{r}}$. Moreover, to simplify the controller design, it is assumed that all system dynamic $L_{f1}(x)$ and $L_{f2}(x)$ are unknown as well. The perturbation terms Ψ_1 and Ψ_2 are defined as

$$\begin{bmatrix} \Psi_1(x) \\ \Psi_2(x) \end{bmatrix} = \begin{bmatrix} L_{f1}(x) \\ L_{f2}(x) \end{bmatrix} + (B(x) - B_0) \begin{bmatrix} u_1 \\ u_2 \end{bmatrix} \tag{11}$$

Thus, the perturbation terms include the system nonlinearities, external disturbances T_{L} and parameter uncertainties.

Then (5) can be rewritten as:

$$\begin{bmatrix} \ddot{y}_1 \\ \ddot{y}_2 \end{bmatrix} = \begin{bmatrix} \Psi_1(x) \\ \Psi_2(x) \end{bmatrix} + B_0 \begin{bmatrix} u_1 \\ u_2 \end{bmatrix} \tag{12}$$

Define new state variables as $z_{i1} = y_i$, $z_{i2} = \dot{y}_i$, and a fictitious state to represent the perturbation terms as $z_{i3} = \Psi_i$ for flux subsystem and speed subsystem, system (12) can be represented as two subsystems as:

$$\begin{cases} \dot{z}_{i1} = z_{i2} \\ \dot{z}_{i2} = z_{i3} + B_{0i} u_i \quad , i = 1, 2 \\ \dot{z}_{i3} = \dot{\Psi}_i \end{cases} \tag{13}$$

Several types of SPO have been proposed for estimating the perturbation terms, such as linear and high-gain observers (Chen et al. (2014)), sliding mode observer (Jiang and Wu (2002)) and nonlinear observer (Han (2009)). In order to achieve the simplest structure and applicability, in this paper SPOs are designed via linear Luenberger observer. The SPO can be designed as:

$$\begin{cases} \dot{\hat{z}}_{i1} = \hat{z}_{i2} + l_{i1} \widetilde{z}_{i1} \\ \dot{\hat{z}}_{i2} = \hat{z}_{i3} + B_{0i} u_i + l_{i2} \widetilde{z}_{i1} \quad , i = 1, 2 \\ \dot{\hat{z}}_{i3} = l_{i3} \widetilde{z}_{i1} \end{cases} \tag{14}$$

where $\hat{z}_{ij}$ are the estimation of z_{ij}, and $\widetilde{z}_{i1} = z_{i1} - \hat{z}_{i1}$ are defined as the state estimation error. The observer gains l_{i1}, l_{i2}, l_{i3} can be parametrised following method (Yoo et al. (2007)):

$$\begin{bmatrix} l_{i1} & l_{i2} & l_{i3} \end{bmatrix} = \begin{bmatrix} 3\alpha_0 & 3\alpha_0^2 & \alpha_0^3 \end{bmatrix} \tag{15}$$

where α_0 is the observer bandwidth and a tuning parameter. The tuning of α_0 should ensure that the observer response is faster than the controlled plant (Yoo et al. (2007)). This leads the observer with larger bandwidth than the bandwidth of the controller plant. On the other hand, the observer should be applied with a lower bandwidth to filter out the measurement sensor noise (Ellis (2002)). Therefore, the observer bandwidth setting should compromise the requirement considering the actual bandwidth of both controller and sensor noise.

3.3. Design of speed observer

3.3.1. Conventional MRAS based speed observer

In the MRAS based speed observer (SO) based on rotor flux equations, the reference model is the rotor flux from the real model calculated by the current feedback, while the adaptive model tracks the rotor flux of the reference model via adjusting the rotor speed (Gadoue et al. (2010)). When the rotor flux difference between adaptive model and reference model eliminated to zero, it is known that the speed estimation is the same with the real speed. The rotor flux dynamics of the reference model can be presented as:

$$\frac{d\psi_{\mathrm{r}\alpha}}{dt} = \frac{L_{\mathrm{r}}}{L_{\mathrm{m}}} v_{\mathrm{s}\alpha} - \frac{L_{\mathrm{r}} R_{\mathrm{s}}}{L_{\mathrm{m}}} i_{\mathrm{s}\alpha} - \frac{\sigma L_{\mathrm{s}} L_{\mathrm{r}}}{L_{\mathrm{m}}} \frac{di_{\mathrm{s}\alpha}}{dt} \tag{16}$$

$$\frac{d\psi_{\mathrm{r}\beta}}{dt} = \frac{L_{\mathrm{r}}}{L_{\mathrm{m}}} v_{\mathrm{s}\beta} - \frac{L_{\mathrm{r}} R_{\mathrm{s}}}{L_{\mathrm{m}}} i_{\mathrm{s}\beta} - \frac{\sigma L_{\mathrm{s}} L_{\mathrm{r}}}{L_{\mathrm{m}}} \frac{di_{\mathrm{s}\beta}}{dt} \tag{17}$$

where the variables $v_{\mathrm{s}\alpha}$, $v_{\mathrm{s}\beta}$, $i_{\mathrm{s}\alpha}$ and $i_{\mathrm{s}\beta}$ are the voltage control inputs and current feedback of real IM.

The rotor flux dynamics of adaptive model is designed to estimate the

rotor flux variables using rotor circuit equations as (Gadoue et al. (2010)):

$$\frac{d\hat{\psi}_{\mathrm{r}\alpha}}{dt} = \frac{L_{\mathrm{m}}}{\tau_{\mathrm{r}}} i_{\mathrm{s}\alpha} - \frac{1}{\tau_{\mathrm{r}}}\hat{\psi}_{\mathrm{r}\alpha} - P\hat{\omega}_{\mathrm{m}}\hat{\psi}_{\mathrm{r}\beta} \tag{18}$$

$$\frac{d\hat{\psi}_{\mathrm{r}\beta}}{dt} = \frac{L_{\mathrm{m}}}{\tau_{\mathrm{r}}} i_{\mathrm{s}\beta} + P\hat{\omega}_{\mathrm{m}}\hat{\psi}_{\mathrm{r}\alpha} - \frac{1}{\tau_{\mathrm{r}}}\hat{\psi}_{\mathrm{r}\beta} \tag{19}$$

where $\hat{\psi}_{\mathrm{r}\alpha}$, $\hat{\psi}_{\mathrm{r}\beta}$ and $\hat{\omega}_{\mathrm{m}}$ are the estimation of rotor flux $\psi_{\mathrm{r}\alpha}$ and $\psi_{\mathrm{r}\beta}$ and mechanical rotor speed ω_{m}, respectively.

The speed tuning signal ϵ is defined as the difference between the rotor fluxes imaginary components from the reference model and adaptive model as Gadoue et al. (2010):

$$\epsilon = \psi_{\mathrm{r}\beta}\hat{\psi}_{\mathrm{r}\alpha} - \psi_{\mathrm{r}\alpha}\hat{\psi}_{\mathrm{r}\beta} \tag{20}$$

Then the adaptation mechanism uses a PI regulator to adjust the estimated rotor speed as:

$$\hat{\omega}_{\mathrm{m}} = k_{\mathrm{P}}\epsilon + k_{\mathrm{I}}\int \epsilon\, dt \tag{21}$$

In the MRAS-SO, as shown in the left side of Figure 1(a), when the error ϵ convergences to zero, the estimated rotor speed $\hat{\omega}_{\mathrm{m}}$ reaches the real speed. Then the estimated rotor speed and rotor flux is used to feed the two SPOs in (14) for perturbation estimation. In the whole controller design, two SPOs are used for state and perturbation estimation of rotor speed and rotor flux in different loops.

3.3.2. Combined speed and perturbation observer

In previous section, a MRAS-SO is designed to estimate the rotor speed and a speed SPO is designed to estimate the speed loop perturbation by using the estimated rotor speed, as shown in the Figure 1 (a). From the

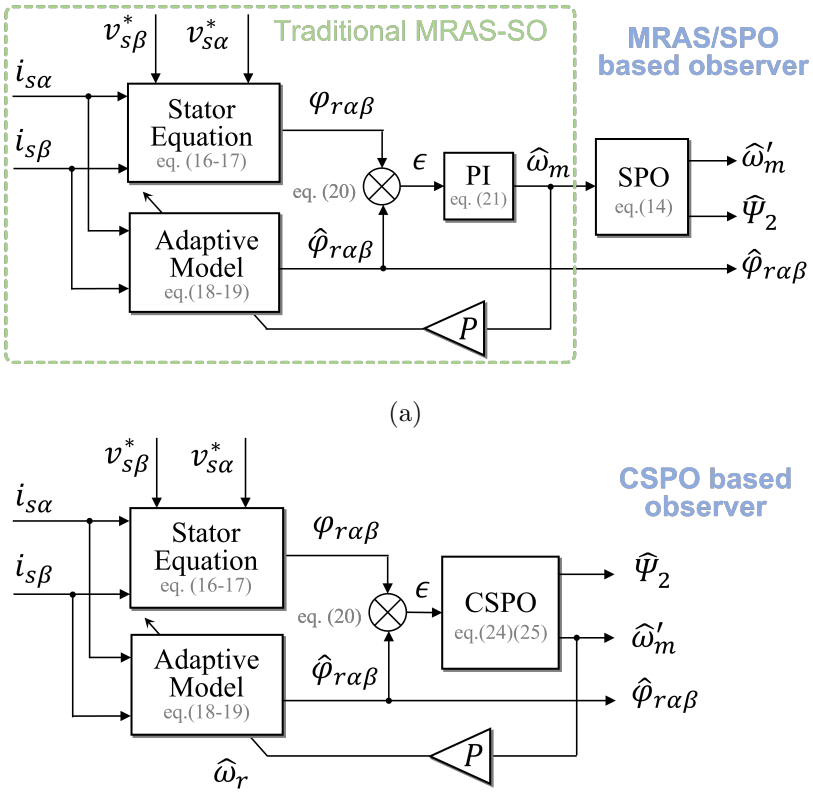

Figure 1: Block diagrams of (a) a traditional MRAS based speed observer and speed perturbation observer, (b) a combined speed and perturbation observer (CSPO).

block diagram, the rotor speed needs to be estimated twice, $\hat{\omega}_{\mathrm{m}}$ and $\hat{\omega}'_{\mathrm{m}}$, in different observers. This undoubtedly increases the computational load.

This section combines the MRAS-SO and speed SPO and proposes a combined speed and perturbation observer (CSPO) that estimates the speed and its perturbation term at the same time, as shown in Figure 1 (b). The motivation of combining the MRAS-SO and speed SPO into a CSPO aims to simplify the work in speed estimation and its perturbation estimation into a simpler define, that when $\epsilon \to 0$, the estimated speed from CSPO tends to the

real rotor speed as $\hat{\omega}'_{\mathrm{m}} \to \omega_{\mathrm{m}}$, and its estimated perturbation $\hat{\Psi}$ tends to its real value at the same time. But in the CSPO, the actual speed signal z_{21} is assuming unknown, and the standard observation error $\widetilde{z}_{21}$ is not achievable. Thus, it is required to find another driving signal to replace the $\widetilde{z}_{21}$ in original speed SPO.

In the original speed SPO, the observer output is driven by the observation error $\widetilde{z}_{21} = z_{21} - \hat{z}_{21}$, where z_{21} comes from the output of PI regulator in the MRAS-SO. In order to simplify the proof, the output of PI is simplified with the product of proportional gain and tuning signal as $z_{21} = k_{\mathrm{P}}\epsilon$. Then speed SPO from equation (14) with $i = 2$ can be rewritten as

$$\begin{cases} \dot{\hat{z}}_{21} = \hat{z}_{22} + l_{21}\left(k_{\mathrm{P}}\epsilon - \hat{z}_{21}\right) \\ \dot{\hat{z}}_{22} = \hat{z}_{23} + B_{02}u_2 + l_{22}\left(k_{\mathrm{P}}\epsilon - \hat{z}_{21}\right) \\ \dot{\hat{z}}_{23} = l_{23}\left(k_{\mathrm{P}}\epsilon - \hat{z}_{21}\right) \end{cases} \tag{22}$$

The above equation can be represented in matrix form as

$$\begin{bmatrix} \dot{\hat{z}}_{21} \\ \dot{\hat{z}}_{22} \\ \dot{\hat{z}}_{23} \end{bmatrix} = \begin{bmatrix} -l_{21} & 1 & 0 \\ -l_{22} & 0 & 1 \\ -l_{23} & 0 & 0 \end{bmatrix} \begin{bmatrix} \hat{z}_{21} \\ \hat{z}_{22} \\ \hat{z}_{23} \end{bmatrix} + \begin{bmatrix} k_{\mathrm{P}}l_{21} \\ k_{\mathrm{P}}l_{22} \\ k_{\mathrm{P}}l_{23} \end{bmatrix} \epsilon + \begin{bmatrix} 0 \\ B_{02}u_2 \\ 0 \end{bmatrix} \tag{23}$$

Thus, it proves that the tuning signal ϵ can be used as the driving signal when $\widetilde{z}_{21}$ is not available. If using Eq. (23) as the CSPO, it will achieve the same performance with MRAS-SO and speed SPO. But this paper aims to reduce the complexity of the direct combination of MRAS-SO and speed SPO. In order to simplify the CSPO design, the proposed CSPO substituted the observation error $\widetilde{z}_{21}$ with the speed tuning signal ϵ from (20). Then the

CSPO can be represented as

$$\begin{cases} \dot{\hat{z}}_{21} = \hat{z}_{22} + l_{21}\epsilon \\ \dot{\hat{z}}_{22} = \hat{z}_{23} + B_{02}u_2 + l_{22}\epsilon \\ \dot{\hat{z}}_{23} = l_{23}\epsilon \end{cases} \tag{24}$$

Comparing among (14), (23) and (24), the CSPO maintains the simplicity of the original SPO, utilizes the tuning signal ϵ to drive the estimation of rotor speed, and replaces the PI regulator in the original MRAS system. In order to verify whether this change is stable, the stability analysis of its closed-loop system will be carried out in later sections.

In the separated approach, the parameters of MRAS-SO and speed SPO are calculated separately. But the parameterisation of CSPO should take into account the stability of both speed estimation and perturbation observation, which is more difficult than the separate MRAS-SO and speed SPO approach. In order to add more degree of freedom in the tuning of system parameters, an additional proportional gain is added to the estimation of rotor speed as

$$\hat{\omega}_{\mathrm{m}} = \hat{z}_{21} + l_{20}\epsilon \tag{25}$$

The final transfer function of the rotor speed estimation can be presented as

$$\hat{\omega}_{\mathrm{m}} = \frac{B_{02}u_2}{s^2} + \left(\frac{l_{23}}{s^3} + \frac{l_{22}}{s^2} + \frac{l_{21}}{s} + l_{20}\right)\epsilon \tag{26}$$

The gains of l_{20}, l_{21}, l_{22} and l_{23} can be achieved by pole placement of the closed-loop system by substituting (25) into system (16) to (19).

Then the CSPO consists of equation (24) and (25) to estimate the rotor speed as well as its perturbation term simultaneously. After the speed tuning

signal ϵ converges to zero, the estimation state $\hat{\omega}_{\mathrm{m}}$ tracks the mechanical rotor speed and $\hat{z}_{23}$ tracks the rotor speed perturbation for speed control and linearising the IM system.

3.4. Speed sensorless nonlinear adaptive controller

In the flux subsystem, the original SPO (14) is used to estimate its perturbation term $\hat{z}_{13}$. In the speed subsystem, the CSPO (24) is used to estimate both the rotor speed $\hat{\omega}_{\mathrm{m}}$ and its perturbation term $\hat{z}_{23}$. Note that the speed can be estimated by a conventional MRAS-SO defined in (16) to (21) and the speed loop perturbation be estimated by a speed SPO defined in (14). Then the control law of the speed sensorless nonlinear adaptive control (SSNAC) can be obtained as:

$$\begin{bmatrix} u_1 \\ u_2 \end{bmatrix} = B_0^{-1} \left(\begin{bmatrix} \upsilon_1 \\ \upsilon_2 \end{bmatrix} - \begin{bmatrix} \hat{z}_{13} \\ \hat{z}_{23} \end{bmatrix} \right) \tag{27}$$

Substituting (27) into (12), the system can be linearised as

$$\begin{aligned} \begin{bmatrix} \ddot{y}_1 \\ \ddot{y}_2 \end{bmatrix} &= \left(\begin{bmatrix} \Psi_1(x) \\ \Psi_2(x) \end{bmatrix} - \begin{bmatrix} \hat{z}_{13} \\ \hat{z}_{23} \end{bmatrix} \right) + \begin{bmatrix} \upsilon_1 \\ \upsilon_2 \end{bmatrix} \\ &= \begin{bmatrix} \upsilon_1 \\ \upsilon_2 \end{bmatrix} + \begin{bmatrix} \widetilde{z}_{13} \\ \widetilde{z}_{23} \end{bmatrix} \end{aligned} \tag{28}$$

where $\widetilde{z}_{i3}$ indicates the SPO estimation error of perturbation term z_{i3} as $\widetilde{z}_{i3} = \Psi_i(\cdot) - \hat{z}_{i3}$.

By compensating the system nonlinear dynamics, parameter uncertainties and external disturbances by the estimated lumped perturbation terms, the linearised system can be easily controlled by lots of developed linear control

law. The linear control law υ_1 and υ_2 can be designed as

$$\begin{cases} \upsilon_1 = \ddot{z}_{11}^* + k_{11}(z_{11}^* - z_{11}) + k_{12}(\dot{z}_{11}^* - \hat{z}_{12}) \\ \upsilon_2 = \ddot{z}_{21}^* + k_{21}(z_{21}^* - z_{21}) + k_{22}(\dot{z}_{21}^* - \hat{z}_{22}) \end{cases} \tag{29}$$

where z_{i1}^* and $\dot{z}_{i1}^*$ are the reference and its derivative of system outputs; k_{i1} and k_{i2} are the gains of linear control law that are determined by pole placement defined as $k_{i1} = n^2$ and $k_{i2} = 2n$ for a given pole location n. The location of poles can be determined for a second-order linear system with a given transient dynamic requirement.

The stator voltages, known as the system control inputs, are calculated from the proposed controller using variables with physical meaning as

$$\begin{cases} v_{\mathrm{sd}} = \dfrac{\sigma L_{\mathrm{s}} \tau_{\mathrm{r}}}{L_{\mathrm{m}}} \left[k_{11}(\psi_r^* - \hat{z}_{11}) + k_{12}(\dot{\psi}_r^* - \hat{z}_{12}) - \hat{z}_{13} \right] \\ v_{\mathrm{sq}} = \dfrac{2J\sigma L_{\mathrm{s}} L_{\mathrm{r}}}{3PL_{\mathrm{m}}\psi_{\mathrm{r0}}} \Big[k_{21} \left(\omega_m^* - \hat{z}_{21} - l_{20} \left(\psi_{\mathrm{r}\beta}\hat{\psi}_{\mathrm{r}\alpha} - \psi_{\mathrm{r}\alpha}\hat{\psi}_{\mathrm{r}\beta} \right) \right) \\ \qquad + k_{22}(\dot{\omega}_m^* - \hat{z}_{22}) - \hat{z}_{23} \Big] \end{cases} \tag{30}$$

The final control scheme of the SSNAC for IM are shown in Figure 2. The SSNAC include two control schemes, the first one is a MRAS-SO/SPOs based SSNAC that includes a conventional MRAS-SO, two SPOs and two control loops for flux and speed subsystem, respectively. The second control scheme is a CSPO based SSNAC that includes the flux SPO, the speed CSPO for and two control loops for flux and speed tracking.

4. Closed-loop Stability Analysis

The previous section proposed two control approaches, the MRAS/SPO based SSNAC and the CSPO based SSNAC. In this section, the stability

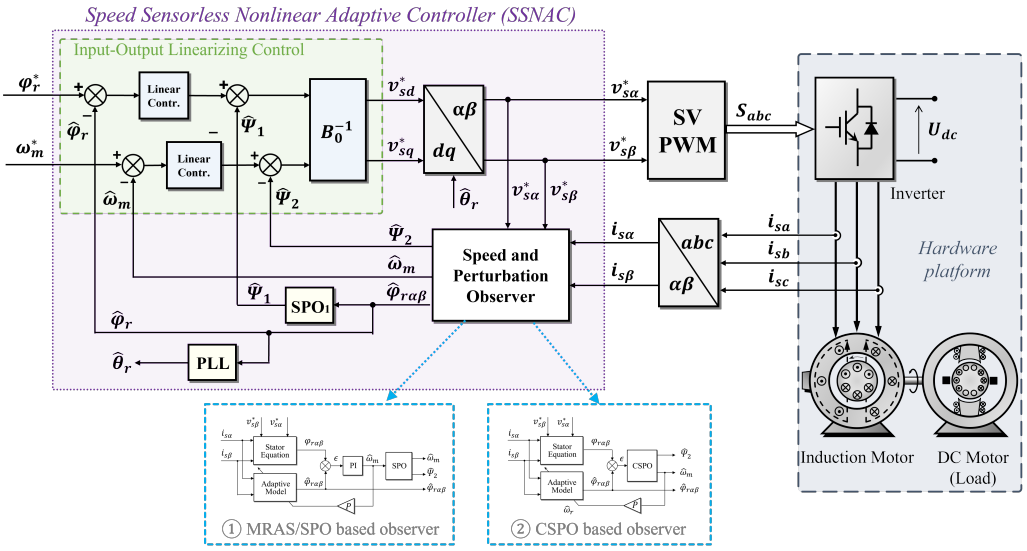

Figure 2: The control scheme of the SSNAC for IM.

analysis of two control schemes has been provided. Section 4.1 and Section 4.2 present the closed-loop stability proof of both control schemes of SSNAC using Lyapunov theory.

4.1. Closed-loop stability of the MRAS/SPO based SSNAC

The closed-loop system includes five subsystems: the MRAS speed observer defined in (16) to (21), the flux and speed perturbation observers defined in (14), and their tracking errors in the IM system.

First, the error dynamic of the MRAS speed observer is obtained with the rotor flux-based speed tuning signal ϵ defined in (20), whose derivative is calculated from the rotor circuit equations as

$$\dot{\epsilon} = -a_1\epsilon + a_2(\omega_{\mathrm{m}} - \hat{\omega}_{\mathrm{m}}) + a_3 \tag{31}$$

where

$$
\begin{aligned}
a_1 &= \frac{2}{\tau_{\mathrm{r}}}, \\
a_2 &= P(\psi_{r\alpha}\hat{\psi}_{\mathrm{r}\alpha} + \psi_{\mathrm{r}\beta}\hat{\psi}_{\mathrm{r}\beta}), \\
a_3 &= \frac{L_{\mathrm{m}}}{\tau_{\mathrm{r}}}(\psi_{\mathrm{r}\beta} - \hat{\psi}_{\mathrm{r}\beta})i_{\mathrm{s}\alpha} - \frac{L_{\mathrm{m}}}{\tau_{\mathrm{r}}}(\psi_{\mathrm{r}\alpha} - \hat{\psi}_{\mathrm{r}\alpha})i_{\mathrm{s}\beta}
\end{aligned} \tag{32}
$$

Combining the adaptation mechanism in (21), the dynamic of speed tuning signal can be rewritten as

$$\dot{\epsilon} = -h_1\epsilon + \lambda \tag{33}$$

where

$$h_1 = a_1 + k_{\mathrm{P}}a_2 \tag{34}$$

$$\lambda = a_2\omega_{\mathrm{m}} + a_3 - k_{\mathrm{I}}\int \epsilon\, dt \tag{35}$$

where h_1 is a positive value as $a_1 > 0$ and $a_2 > 0$ (as proved in the Appendix A) and $k_P > 0$ defined in (21).

Second, define the estimation error of the flux SPO and the speed SPO as $\widetilde{z}_{i1} = z_{i1} - \hat{z}_{i1}$, $\widetilde{z}_{i2} = z_{i2} - \hat{z}_{i2}$, and $\widetilde{z}_{i3} = \Psi_i(\cdot) - \hat{z}_{i3}$, where $i = 1$ indicating the flux SPO and $i = 2$ indicating the speed SPO. The error dynamic of flux SPO and speed SPO are obtained from (13) and (14) as

$$\begin{bmatrix} \dot{\widetilde{z}}_{i1} \\ \dot{\widetilde{z}}_{i2} \\ \dot{\widetilde{z}}_{i3} \end{bmatrix} = \begin{bmatrix} -l_{i1} & 1 & 0 \\ -l_{i2} & 0 & 1 \\ -l_{i3} & 0 & 0 \end{bmatrix} \begin{bmatrix} \widetilde{z}_{i1} \\ \widetilde{z}_{i2} \\ \widetilde{z}_{i3} \end{bmatrix} + \begin{bmatrix} 0 \\ 0 \\ \dot{\Psi}_1(\cdot) \end{bmatrix} \tag{36}$$

Then (36) can be rewritten in matrix format as

$$[\dot{\widetilde{z}}_i] = [A_i][\widetilde{z}_i] + [\eta_i] \tag{37}$$

where $[A_i]$ is the non-singular observer parameter matrix for both SPOs and $[\widetilde{z}_i] = [\widetilde{z}_{i1} \quad \widetilde{z}_{i2} \quad \widetilde{z}_{i3}]^T$ is the vector of estimation error with and $[\eta_i] = [0 \quad 0 \quad \dot{\Psi}_i]^T$ indicate the vector of derivatives of perturbation terms.

The perturbation terms Ψ_i depend on the system parameters and variations, system input and external disturbance. In the IM, the system parameters and their variations have to be bounded. The system inputs are given by the control outputs which are designed to be bounded. The external torque disturbance cannot be guaranteed to be bounded, but infinite external torque disturbance is out of the scope of the controller design. Due to these, the derivatives of the perturbation terms $\dot{\Psi}_i$ are considered as bounded in this paper as a precondition.

Third, define the system output tracking error as $e_{i1} = y_i^* - z_{i1}$ and $e_{i2} = \dot{y}_i^* - z_{i2}$, where $i = 1$ indicating the flux control loop and $i = 2$ indicating the speed control loop. The control law in (29) can then be represented as:

$$\begin{aligned} \upsilon_i &= k_{i1}(y_i^* - z_{i1} + z_{i1} - \hat{z}_{i1}) + k_{i2}(\dot{y}_i^* - z_{i2} + z_{i2} - \hat{z}_{i2}) \\ &= k_{i1}(e_{i1} + \widetilde{z}_{i1}) + k_{i2}(e_{i2} + \widetilde{z}_{i2}) \end{aligned} \tag{38}$$

From (12) and (38), the closed-loop tracking error dynamics are obtained as

$$\begin{bmatrix} \dot{e}_{i1} \\ \dot{e}_{i2} \end{bmatrix} = \begin{bmatrix} 0 & 1 \\ -k_{i1} & -k_{i2} \end{bmatrix} \begin{bmatrix} e_{i1} \\ e_{i2} \end{bmatrix} + \begin{bmatrix} 0 \\ -\xi_i \end{bmatrix} \tag{39}$$

where

$$\xi_i = \begin{bmatrix} k_{i1} & k_{i2} & 1 \end{bmatrix} \times \begin{bmatrix} \widetilde{z}_{i1} \\ \widetilde{z}_{i2} \\ \widetilde{z}_{i3} \end{bmatrix} \tag{40}$$

which indicates the lumped estimation error from (36).

Similarly, rewrite system (39) in the matrix format as

$$[\dot{e}_i] = [M_i][e_i] + [K_i][\widetilde{z}_i] \tag{41}$$

where $[e_i] = [e_{i1} \quad e_{i2}]^T$ indicates the tracking error of the closed-loop system; $[M_i]$ is the non-singular controller parameter matrix of flux and speed subsystems; $[K_i]$ is the matrix depending on control gains.

For the stability proof, assuming that the system input gain $B(x)$ and its derivative are bounded and $B(x)$ is non-singular when $\psi_r \neq 0$; and the perturbation terms $\Psi_i(x,t)$ and their derivatives $\dot{\Psi}_i(x,t)$ are bounded. This assumption is reasonable based on the fact that the target system is a physical system containing mechanical and electrical processes, so its variables will be within a suitable range instead of infinite values. Then the closed-loop error system can be proved to be globally uniformly ultimately bounded (GUUB) as the following theorem.

Theorem 1. *Consider the IM system (1) equipped the proposed SSNAC (30) with the MRAS-SO in (16) to (21) and two SPOs in (14). If the perturbation terms $\Psi_i(x,t)$ defined in (11) satisfying*

$$\begin{cases} \|\dot{\Psi}_1(x,t)\| \leq \gamma_1 \\ \|\dot{\Psi}_2(x,t)\| \leq \gamma_2 \end{cases} \tag{42}$$

then the estimation error in (33) and (36) and the tracking error in (41) are

GUUB, i.e.,

$$\begin{cases} |\epsilon(t)| \leq P_1|\lambda| \\ \|[\widetilde{z}_1](t)\| \leq 2\gamma_1\|[P_{21}]\| \\ \|[\widetilde{z}_2](t)\| \leq 2\gamma_2\|[P_{22}]\| & ,\forall t \geq T \\ \|[e_1](t)\| \leq 4\gamma_1\|[K_1]\|\|[P_{21}]\|\|[P_{31}]\| \\ \|[e_2](t)\| \leq 4\gamma_2\|[K_2]\|\|[P_{22}]\|\|[P_{32}]\| \end{cases} \tag{43}$$

Proof. For the error variable ϵ in (33), choose a Lyapunov function as $V_{\text{so}}(\epsilon) = \frac{1}{2}P_1\epsilon^2$. The h_1 defined in (34) is a positive value, the P_1 can be set as a positive value of $P_1 = h_1^{-1}$.

For the SPOs estimation error $[\widetilde{z}_i]$ in (37), choose the Lyapunov function as $V_{\text{spo},i}([\widetilde{z}_i]) = [\widetilde{z}_i]^{\text{T}}[P_{2i}][\widetilde{z}_i]$. The gains of SPOs (14) are determined by (15), which means $[A_i]$ is Hurwitz. Then a feasible positive solution $[P_{2i}]$ can be found from the Riccati equation $[A_i]^{\text{T}}[P_{2i}] + [P_{2i}][A_i] = -I$.

For the tracking error $[e_i]$ in (41), define a Lyapunov function $V_{\text{t},i}([e_i]) = [e_i]^{\text{T}}[P_{3i}][e_i]$ and a $[P_{3i}]$ as a feasible positive solution from the Riccati equation $[M_i]^{\text{T}}[P_{3i}] + [P_{3i}][M_i] = -I$.

The Lyapunov function of closed-loop system can be defined as the sum of MRAS speed observer, two SPOs, and two control loops as $V(\epsilon, [\widetilde{z}_1], [\widetilde{z}_2], [e_1], [e_2]) = V_{\text{so}}(\epsilon) + V_{\text{spo},1}([\widetilde{z}_1]) + V_{\text{spo},2}([\widetilde{z}_2]) + V_{\text{t},1}([e_1]) + V_{\text{t},2}([e_2])$. Then the derivative

of V can be obtained as

$$\begin{aligned}
\dot{V} &= P_1\epsilon(-h_1\epsilon+\lambda)+[\widetilde{z}_1]^{\mathrm{T}}([A_1]^{\mathrm{T}}[P_{21}]+[P_{21}][A_1])[\widetilde{z}_1] \\
&\quad +[\widetilde{z}_2]^{\mathrm{T}}([A_2]^{\mathrm{T}}[P_{22}]+[P_{22}][A_2])[\widetilde{z}_2] \\
&\quad +[e_1]^{\mathrm{T}}([M_1]^{\mathrm{T}}[P_{31}]+[P_{31}][M_1])[e_1] \\
&\quad +[e_2]^{\mathrm{T}}([M_2]^{\mathrm{T}}[P_{32}]+[P_{32}][M_2])[e_2] \\
&\leq -\epsilon^2+P_1|\epsilon||\lambda|-\|[\widetilde{z}_1]\|^2+2\|[\widetilde{z}_1]\|\|[\eta_1]\|\|[P_{21}]\|-\|[\widetilde{z}_2]\|^2 \\
&\quad +2\|[\widetilde{z}_2]\|\|[\eta_2]\|\|[P_{22}]\|-\|[e_1]\|^2+2\|[e_1]\|\|[K_1]\|\|[\widetilde{z}_1]\|\|[P_{31}]\| \\
&\quad -\|[e_2]\|^2+2\|[e_2]\|\|[K_2]\|\|[\widetilde{z}_2]\|\|[P_{32}]\| \\
&\leq -|\epsilon|\left(|\epsilon|-P_1|\lambda|\right)-\|[\widetilde{z}_1]\|\left(\|[\widetilde{z}_1]\|-2\gamma_1\|[P_{21}]\|\right) \\
&\quad -\|[\widetilde{z}_2]\|\left(\|[\widetilde{z}_2]\|-2\gamma_2\|[P_{22}]\|\right) \\
&\quad -\|[e_1]\|\left(\|[e_1]\|-2\|[K_1]\|\|[\widetilde{z}_1]\|\|[P_{31}]\|\right) \\
&\quad -\|[e_2]\|\left(\|[e_2]\|-2\|[K_2]\|\|[\widetilde{z}_2]\|\|[P_{32}]\|\right)
\end{aligned} \tag{44}$$

Each Lyapunov function in (44) has its own close-loop. In the first section, as λ defined in (35) is bounded (as proved in Appendix B), when $|\epsilon|>P_1|\lambda|$, the $-|\epsilon|\left(|\epsilon|-P_1|\lambda|\right)\leq 0$ can be obtained. Thus, there exists a time $T_1>0$ to satisfy

$$|\epsilon(t)|\leq P_1|\lambda|, \quad \forall t\geq T_1 \tag{45}$$

Similarly, there exists T_2 and T_3 to satisfy

$$\|[\widetilde{z}_1](t)\|\leq 2\gamma_1\|P_{21}\|, \quad \forall t\geq T_2 \tag{46}$$

$$\|[\widetilde{z}_2](t)\|\leq 2\gamma_2\|P_{22}\|, \quad \forall t\geq T_3 \tag{47}$$

and T_3 and T_4 to satisfy

$$\|[e_1](t)\|\leq 4\gamma_1\|K_1\|\|P_{21}\|\|P_{31}\|, \quad \forall t\geq T_4 \tag{48}$$

$$\|[e_2](t)\|\leq 4\gamma_2\|K_2\|\|P_{22}\|\|P_{32}\|, \quad \forall t\geq T_5 \tag{49}$$

Considering (45) to (49) to give $T = \max(T_1, T_2, T_3, T_4, T_5)$ to lead (43). It proved that the closed-loop system of using the separate SO and speed SPO is stable and the speed estimation error, the flux and speed perturbation estimation error and tracking error are bounded.

4.2. Closed-loop stability of the CSPO based SSNAC

In another SSNAC approach that uses the CSPO, its dynamics is obtained from the MRAS error defined in (33) to (35) and speed SPO in (36) into a single matrix as

$$\begin{bmatrix} \dot{\epsilon} \\ \dot{\widetilde{z}}_{21} \\ \dot{\widetilde{z}}_{22} \\ \dot{\widetilde{z}}_{23} \end{bmatrix} = \begin{bmatrix} -a_1 - l_{20}a_2 & a_2 & 0 & 0 \\ -l_{21} & 0 & 1 & 0 \\ -l_{22} & 0 & 0 & 1 \\ -l_{23} & 0 & 0 & 0 \end{bmatrix} \begin{bmatrix} \epsilon \\ \widetilde{z}_{21} \\ \widetilde{z}_{22} \\ \widetilde{z}_{23} \end{bmatrix} + \begin{bmatrix} a_3 \\ 0 \\ 0 \\ \dot{\Psi}_2(\cdot) \end{bmatrix} \tag{50}$$

where a_1 and a_2 are positive values defined in (32) and $-a_1 - l_{20}a_2$ can be adjusted by gain l_{20}.

The error system (50) can be rewritten into matrix form as

$$[\dot{\widetilde{z}}_3] = [\Lambda][\widetilde{z}_3] + [\delta] \tag{51}$$

With the new estimation error (51), the (41) of speed subsystem can be rewritten as

$$[\dot{e}_2] = [M_2][e_2] + [K_3][\widetilde{z}_3] \tag{52}$$

where

$$[K_3] = \begin{bmatrix} 0 & k_{21} & k_{22} & 1 \end{bmatrix} \tag{53}$$

The following theorem is summarised.

Theorem 2. *Consider the IM system (1) equipped the proposed SSNAC (30) with a flux SPO in (14) and a CSPO in (24). If the perturbation terms $\Psi_i(x,t)$ defined in (11) is bounded as in (42), then the estimation error in (50) and the tracking error in (41) are GUUB, i.e.,*

$$\begin{cases} \|[\widetilde{z}_1](t)\| \leq 2\gamma_1 \|[P_{21}]\| \\ \|[\widetilde{z}_3](t)\| \leq 2\gamma_2 \|[P_4]\| \\ \|[e_1](t)\| \leq 4\gamma_1 \|[K_1]\| \|[P_{21}]\| \|[P_{31}]\| \\ \|[e_2](t)\| \leq 4\gamma_3 \|[K_3]\| \|[P_4]\| \|[P_{32}]\| \end{cases}, \forall t \geq \bar{T} \tag{54}$$

where $\gamma_3 = \max\{a_3, \gamma_2\}$.

Proof. Define the Lyapunov function for (51) as $V_{\text{cspo}}([\widetilde{z}_3]) = [\widetilde{z}_3]^{\text{T}}[P_4][\widetilde{z}_3]$, where $[P_4]$ is a feasible positive solution from the Riccati equation $[\Lambda]^{\text{T}}[P_4] + [P_4][\Lambda] = -I$.

The Lyapunov function of closed-loop system can be defined as the sum of the flux SPO, CSPO and two control loops as $\bar{V}([\widetilde{z}_1], [\widetilde{z}_3], [e_1], [e_2]) = V_{\text{spo},1} + V_{\text{cspo}}([\widetilde{z}_3]) + V_{\text{t},1}([e_1]) + V_{\text{t},2}([e_2])$. Then the derivative of $\bar{V}$ can be

obtained as

$$\begin{aligned}
\dot{\bar{V}} &= [\widetilde{z}_1]^{\mathrm{T}}([A_1]^{\mathrm{T}}[P_{21}] + [P_{21}][A_1])[\widetilde{z}_1] \\
&\quad +[\widetilde{z}_3]^{\mathrm{T}}([\Lambda]^{\mathrm{T}}[P_4] + [P_4][\Lambda])[\widetilde{z}_3] \\
&\quad +[e_1]^{\mathrm{T}}([M_1]^{\mathrm{T}}[P_{31}] + [P_{31}][M_1])[e_1] \\
&\quad +[e_2]^{\mathrm{T}}([M_2]^{\mathrm{T}}[P_{32}] + [P_{32}][M_2])[e_2] \\
&\leq -\|[\widetilde{z}_1]\|^2 + 2\|[\widetilde{z}_1]\|\|[\eta]\|\|[P_{21}]\| \\
&\quad -\|[\widetilde{z}_3]\|^2 + 2\|[\widetilde{z}_3]\|\|[\delta]\|\|[P_4]\| \\
&\quad -\|[e_1]\|^2 + 2\|[e_1]\|\|[K_1]\|\|[\widetilde{z}_1]\|\|[P_{31}]\| \\
&\quad -\|[e_2]\|^2 + 2\|[e_2]\|\|[K_3]\|\|[\widetilde{z}_3]\|\|[P_{32}]\| \\
&\leq -\|[\widetilde{z}_1]\|\left(\|[\widetilde{z}_1]\| - 2\gamma_1\|[P_{21}]\|\right) \\
&\quad -\|[\widetilde{z}_3]\|\left(\|[\widetilde{z}_3]\| - 2\gamma_3\|[P_4]\|\right) \\
&\quad -\|[e_1]\|\left(\|[e_1]\| - 2\|[K_1]\|\|[\widetilde{z}_1]\|\|[P_{31}]\|\right) \\
&\quad -\|[e_2]\|\left(\|[e_2]\| - 2\|[K_3]\|\|[\widetilde{z}_3]\|\|[P_{32}]\|\right)
\end{aligned} \tag{55}$$

Similarly, there exists $\bar{T}_3$ to satisfy

$$\|[\widetilde{z}_3](t)\| \leq 2\gamma_3\|P_4\|, \quad \forall t \geq \bar{T}_3 \tag{56}$$

and $\bar{T}_5$ to satisfy

$$\|[e_2](t)\| \leq 4\gamma_3\|K_3\|\|P_4\|\|P_{32}\|, \quad \forall t \geq \bar{T}_5 \tag{57}$$

Considering (46), (48), (56) and (57) to give $\bar{T} = \max\left(T_2, \bar{T}_3, T_4, \bar{T}_5\right)$ to lead (54).

This verifies that the closed-loop system is stable and the estimation error of flux SPO and speed CSPO and tracking error of flux and speed are bounded.

Besides, if $[\delta]$ is locally Lipschitz, the observation error and tracking error can be guaranteed the exponential convergence (Jiang and Wu (2002)) and finally to give

$$\lim_{t\to\infty} \epsilon(t) = 0, \quad \lim_{t\to\infty} \widetilde{z}_{ij}(t) = 0 \quad \text{and} \quad \lim_{t\to\infty} e_{ik}(t) = 0 \tag{58}$$

where $i = 1, 2$ indicates different subsystems, $j = 1, 2, 3$ indicates the state orders in estimation and $k = 1, 2$ indicates the state orders in controller.

This guarantees that the estimation error from both the MRAS speed estimator and SPOs and the close-loop error produced by the unknown disturbance are finally converged to zero to make the IM system stable.

The internal dynamic of the IM system is anlysed uding a zero-dynamic technique. In zero-dynamic, the estimated speed and rotor flux as well as their derivatives are well controlled, i.e. $[e] + [\widetilde{z}] = 0$ and $[\dot{e}] + [\dot{\widetilde{z}}] = 0$ in (38), the estimated states tracks their real value as $\hat{z}_{ij} = z_{ij}$ and system outputs track their reference as $z_{i1} = y_i^*$. Thus, the system outputs can be represented as $\omega_{\mathrm{m}} = \omega_{\mathrm{m}}^*$, $\psi_{\mathrm{r}} = \psi_{\mathrm{r}}^*$, $\dot{\omega}_{\mathrm{m}} = 0$, $\dot{\psi}_{\mathrm{r}} = 0$, $\hat{z}_{i1} = y_i^*$ and $\hat{z}_{i3} = \Psi_i$. Then combining with (5) to (8), the control inputs defined in (30) can be represented as

$$\begin{cases} v_{\mathrm{sd0}} = \left(R_{\mathrm{s}} + \dfrac{R_{\mathrm{r}}L_{\mathrm{s}}}{L_{\mathrm{r}}}\right) i_{\mathrm{sd}} - \sigma L_{\mathrm{s}}\omega_{\mathrm{e}} i_{\mathrm{sq}} - \dfrac{L_{\mathrm{s}}}{L_{\mathrm{m}}\tau_{\mathrm{r}}}\psi_{\mathrm{r}}^* \\ v_{\mathrm{sq0}} = \left(R_{\mathrm{s}} + \dfrac{R_{\mathrm{r}}L_{\mathrm{s}}}{L_{\mathrm{r}}}\right) i_{\mathrm{sq}} + \sigma L_{\mathrm{s}}\omega_{\mathrm{e}} i_{\mathrm{sd}} + \dfrac{P\omega_{\mathrm{m}}L_{\mathrm{m}}}{L_{\mathrm{r}}}\psi_{\mathrm{r}}^* - \dfrac{\sigma L_{\mathrm{s}}L_{\mathrm{m}}R_{\mathrm{r}}}{L_{\mathrm{r}}\psi_{\mathrm{r}}^*} i_{\mathrm{sd}} i_{\mathrm{sq}} \end{cases} \tag{59}$$

Substitute (59) into the original IM system (1), one can derive that $\dot{i}_{\mathrm{sd}} = 0$ and $\dot{i}_{\mathrm{sd}} = 0$ and the steady state currents can be obtained as

$$\lim_{t\to\infty} i_{\mathrm{sd}}(t) = \frac{\psi_{\mathrm{r}}^*}{L_{\mathrm{m}}} \tag{60}$$

$$\lim_{t\to\infty} i_{\mathrm{sq}}(t) = \frac{2T_{\mathrm{L}}L_{\mathrm{r}}}{3PL_{\mathrm{m}}\psi_{\mathrm{r}}^{*}} \tag{61}$$

After the states ω_{m} and ψ_{r} and their derivatives are stable, the corresponding states, such as the stator currents i_{sd} and i_{sq}, are also stable. The zero-dynamic of the internal system of IM is stable and, therefore, the closed-loop system error dynamics is stable as well.

5. Simulation Results

The control performance of SSNAC for IM is verified in simulation using MATLAB/Simulink and in hardware implementation on dSPACE hardware platform. The simulation tests are carried out in the time-continuous domain for both the observer and controllers. At first, in order to validate the effectiveness of the CSPO, the speed estimation performance of NAC with separated traditional MRAS speed observer and SSNAC with CSPO are compared in simulation study. As the MRAS speed estimator is parameter sensitive, the variation of IM parameters has been tested of both the rotor resistance and load torque in order to test the performance reduction of the speed sensorless approach affected by parameter variation. After that, the case studies of forward and reverse motoring and time-varying load torque disturbance have been given in both the software simulation and hardware implementation. The parameters of target IM system have been given in Table 1. The controller parameters of SSNAC as well as two SPOs are listed in Table 2.

Table 1: System parameters of IM

Parameter	Value	Unit
R_{s}	0.1607	Ω
R_{r}	0.1690	Ω
L_{s}	6.017	mH
L_{r}	5.403	mH
L_{m}	5.325	mH
J	0.000145	kg
P	2	

Table 2: Controller parameters of SSNAC

Name	Parameter & Value
Flux SPO	$l_{11} = 9 \times 10^3$
	$l_{12} = 2.7 \times 10^7$
	$l_{13} = 2.7 \times 10^9$
Speed SPO	$l_{20} = 2 \times 10^3$
	$l_{21} = 6 \times 10^3$
	$l_{22} = 1.2 \times 10^7$
	$l_{23} = 8 \times 10^9$
Flux Controller	$k_{11} = 1.5 \times 10^4$
	$k_{12} = 2.5 \times 10^2$
Speed Controller	$k_{21} = 1 \times 10^4$
	$k_{22} = 2 \times 10^2$

5.1. Sensorless speed tracking performance test

This test aims to verify the effectiveness of using CSPO to replace the PI based adaptation mechanism in conventional MRAS speed observer. The comparison between separated MRAS-SO plus speed SPO and CSPO in simulation result is shown in Figure 3. The result demonstrates that both the

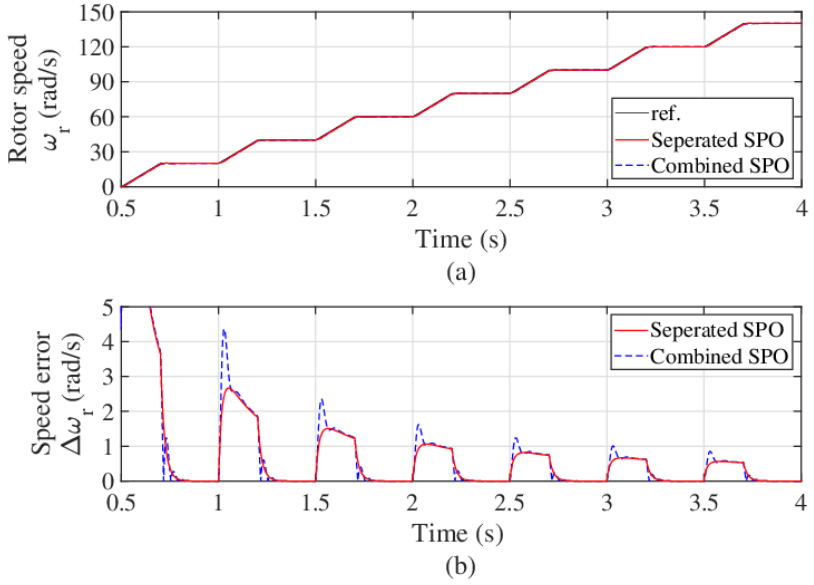

Figure 3: Speed tracking performance comparison between seperated SPO and combined SPO.

separated SO plus speed SPO and CSPO has good performance in estimating the rotor speed from 0 to 150 rad/s. In Figure 3 (b), the comparison of estimation error shows that the speed estimation performs better in higher speed than lower speed in both method. As the separated MRAS-SPO and CSPO has similar performance in speed estimation, only the results of CSPO based SSNAC are presented in all the following case studies.

5.2. Sensitivity test to parameter variation

In IM systems, the rotor resistances are typically uncertain since they are possible varied during operations due to rotor heating, especially in the wound-rotor IMs (Marino et al. (2005); Li et al. (2015)). The SSNAC under varied rotor resistance have been validated in simulation. The result of SSNAC under different constant rotor resistance variation and a rated con-

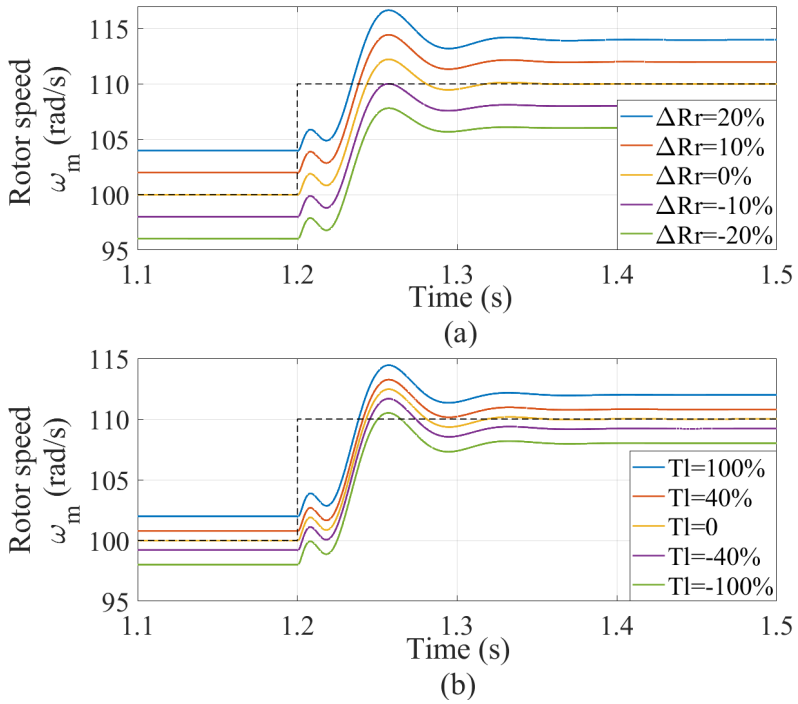

Figure 4: Simulation result of SSNAC under (a) rated load torque and different rotor resistance variation, and (b) 10% mismatch of rated rotor resistance and different load torque.

stant load torque has been shown in Figure 4 (a), and that of a constant 10% rotor resistance variation and different load torque has been shown in Figure 4 (b). When the rotor resistance varies with a constant mismatch to its normal value, the speed controller performs the same dynamic response. Up to 20% mismatching of R_r have been tested, with the estimation performance degraded and steady-state shift with less than 4% estimation error, which is acceptable. Thus, under a constant uncertain load torque and rotor resistance, the dynamic response and stability of an IM controlled by SSNAC will not be affected.

5.3. Speed tracking under constant load disturbance

In the IM application, the speed tracking under constant load is the most common condition. Figure 5 shows the result of different control methods for speed tracking under constant load, which can be either positive or negative load torque. In the test case, from t=1.0 s to t=2.0 s, the load torque rises from 0 to 0.4 Nm and keep constant. The rotor speed rises from 0 to 80 rad/s and stays at this speed. After the speed reached the steady state, the load torque reduced from positive to negative 0.4 Nm. During this period, the IM should also be able to keep the speed. At last, from t=6.0 s, the IM start to decelerate from 80 rad/s to 0 under the negative load applied on the rotor. The load torque is shown as in Figure 5(a) and the rotor speed is shown as in Figure 5(b). As the rotor speed is under the limit of the rated value, the IM is not using in the field weakening area. Thus, the flux reference is set to constant in its rated value at 0.0265 Wb during the speed tracking. The rotor flux is shown in Figure 5(c).

In the control performance of rotor speed and rotor flux, it can be obviously found that the SSNAC tracks reference better than that of traditional speed sensorless method of VC with MRAS speed observer. In order to compare their relative tracking error, Figure 5(d) and 5(e) show the tracking error of rotor speed and rotor flux in percentage. In the comparison, the maximum speed error of SSNAC is less than 1% at t=4.5 s while the maximum speed error of VC plus MRAS is around 8% caused by the load disturbance changed from positive to negative. When rotor speed is rising or decreasing, the control performance of SSNAC is also better than the traditional control method with faster error elimination. The result of rotor flux tracking error

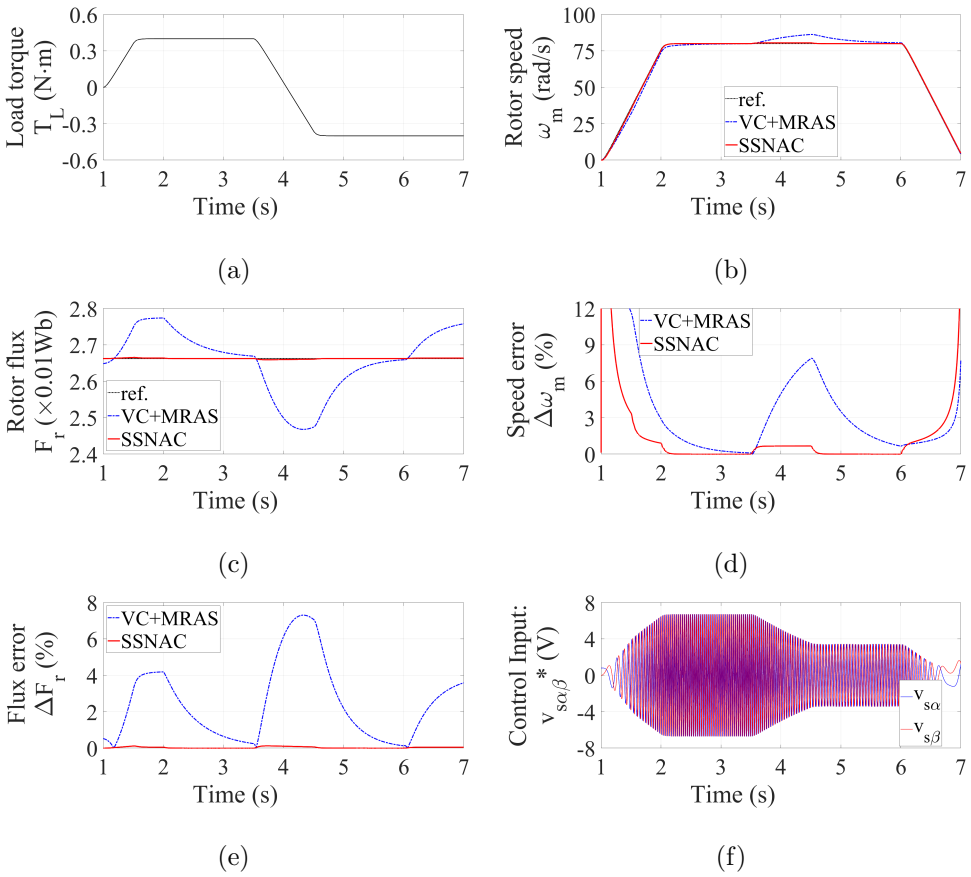

Figure 5: Simulation results of IM speed tracking under constant load disturbance. (a) Load disturbance, (b) rotor speed, (c) rotor flux, (d) speed tracking error, (e) flux tracking error, and (f) stator voltage control input of SSNAC.

also shows that the SSNAC obviously reduced the flux tracking error caused by varying of speed and load disturbance. In order to compare the control performance numerically, the detailed indices are given in Table 3. The control input of stator voltage of SSNAC is given in Figure 5(f), which shows that even the SSNAC performs much better in speed and flux tracking, the control actuator is not over used as the stator voltage is within its limit.

As the indices summarised in Table 3, the maximum flux error of SSNAC

is 98% less than that of the traditional VC plus MRAS method while the flux integral-absolute-error (IAE) of SSNAC has reduced 99%. In the speed tracking indices, the maximum speed error and IAE of speed regulation are reduced by 79% and 81%, respectively.

Even though the control performance has been validated as improved a lot, the estimation performance of the CSPO will need to be tested. Figure 6(a) shows the speed estimation result in rotor speed tracking. The absolute speed estimation error is shown in Figure 6(b). The result of speed estimation shows that the maximum estimation error is less than 0.01 rad/s in speed acceleration and deceleration. When the load changes from positive to negative, the maximum estimation error is less than 0.004 rad/s at the speed of 80rad/s. The reason of which is the absolute accuracy of model and parameters between reference and adaptive model. But in practice, it is difficult to obtain the exact model as well as its accurate parameters.

The effectiveness of perturbation estimating and compensating also needs to be verified. Figure 6(c) and 6(e) show the estimation performance of perturbation terms of flux and speed, where the real value of perturbation terms in the nonlinear IM system is presented by the solid green lines and the estimated perturbation terms from SPOs are presented by the dashed red line. Their estimation errors are given in Figure 6(d) and 6(f). The result shows that the average estimation error of flux perturbation term of around 2% and that of speed perturbation term is around 0.3%.

5.4. Time-varying load torque disturbance test

After the speed tracking under constant load disturbance has been tested, another most common case is the constant speed regulation under time-

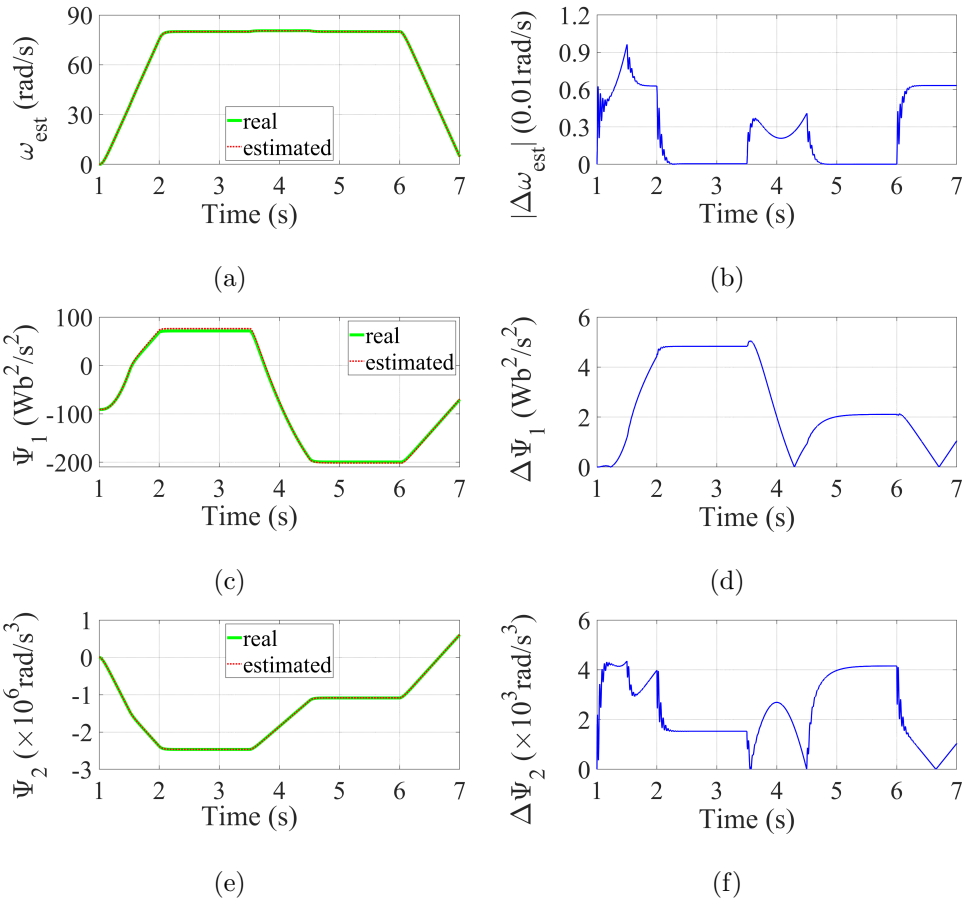

Figure 6: Estimation performance of the CSPO under constant load disturbance speed tracking.

varying load torque as unknown external disturbance. In this case, both the speed and flux are expected to be kept constant, but the load disturbance is time-varying and fast changes. This is to verify the stability of the control system under continuous disturbances. From the start, the rotor speed is rising and stays at 100 rad/s. Then at t=4 s, the load torque applied on IM with a sharp vibration in sinewave with amplitude of 0.3 Nm and frequency of 0.5 Hz, as shown in Figure 7(a).

The control performance of rotor speed and rotor flux regulation are shown in Figure 7(b) and 7(c). Both the SSNAC and traditional VC plus MRAS are affected by the load disturbance with speed sharply reduced. Then the SSNAC responses fast to regulate the rotor speed back to its reference while the traditional VC plus MRAS method has larger regulation error. The flux regulation performance is more obvious that the time-varying load has less impact to the SSNAC as it fully decoupled the interaction between speed and flux. The relative regulation errors of rotor flux and rotor speed are shown in Figure 7(d) and 7(e). And Figure 7(f) shows the stator voltage of SSNAC as its control inputs. In the speed tracking error, an interesting finding is the phase leading of SSNAC to VC plus MRAS due to the estimation and compensation of perturbation terms that includes the prediction of load torque. The performance indices are also summarised in Table 3, in which it shows that the SSNAC reduced the maximum regulation error of flux and speed by 99% and 87% and reduced the IAE of flux and speed by 99% and 88%, respectively.

The speed estimation performance of the CSPO is shown in Figure 8(a) and its estimation error is shown in Figure 8(b). The result shows that the maximum estimation error is less than 0.009 rad/s under the speed of 100 rad/s. That is also because of the accurate model and parameters used. The two lumped perturbation terms of flux and rotor speed are estimated and compared with their real value in Figure 8(c) and 8(e) while their estimation error are given in Figure 8(d) and 8(f). The average estimation error of perturbation term of flux is around 2% and that of speed is around 0.8%. Thus, the perturbation terms are well estimated to compensate their real

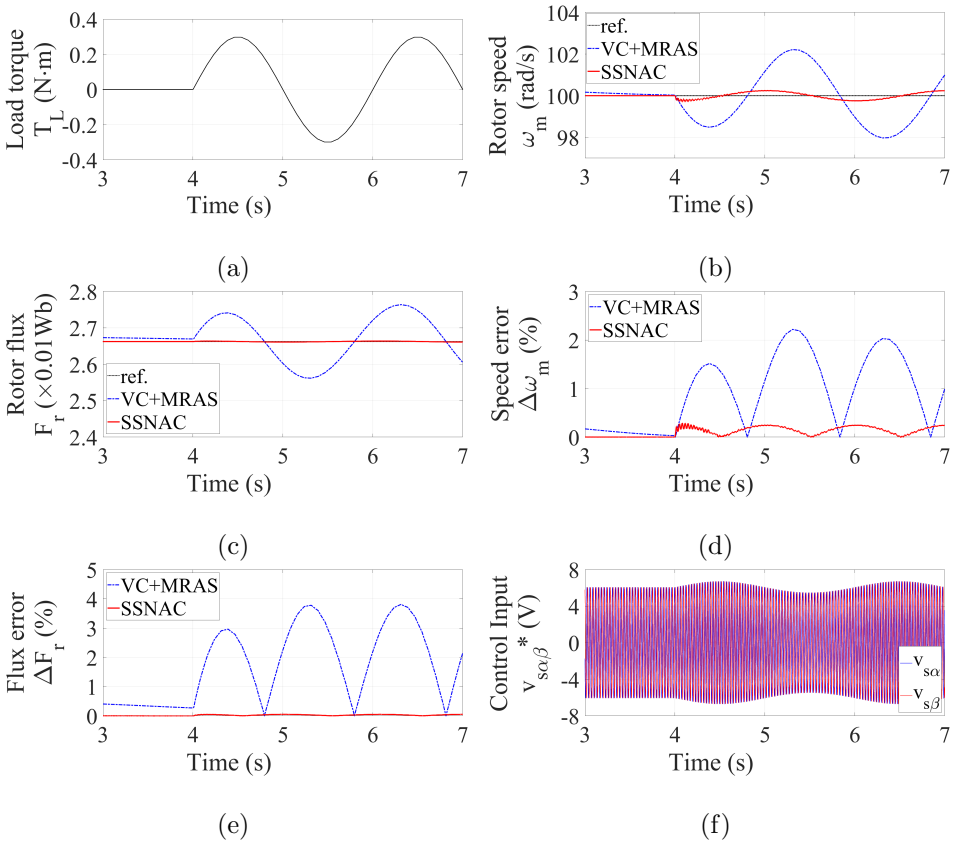

Figure 7: Simulation results of IM constant speed regulation under time-varying load torque disturbance. (a) Load disturbance, (b) rotor speed, (c) rotor flux, (d) speed tracking error, (e) flux tracking error, and (f) stator voltage control input.

value for fully linearise the coupled states in the nonlinear IM system.

6. Experiment Results

6.1. Experimental platform

The experimental setup of SSNAC for IM hardware implementation is shown in Figure 9. The target motor is a 200 W, 2 pole pairs, three phase wound-rotor IM from Motorsolver. Other devices include a 42 V power electronics (PE) converter unit and current transducers, two power supplies to

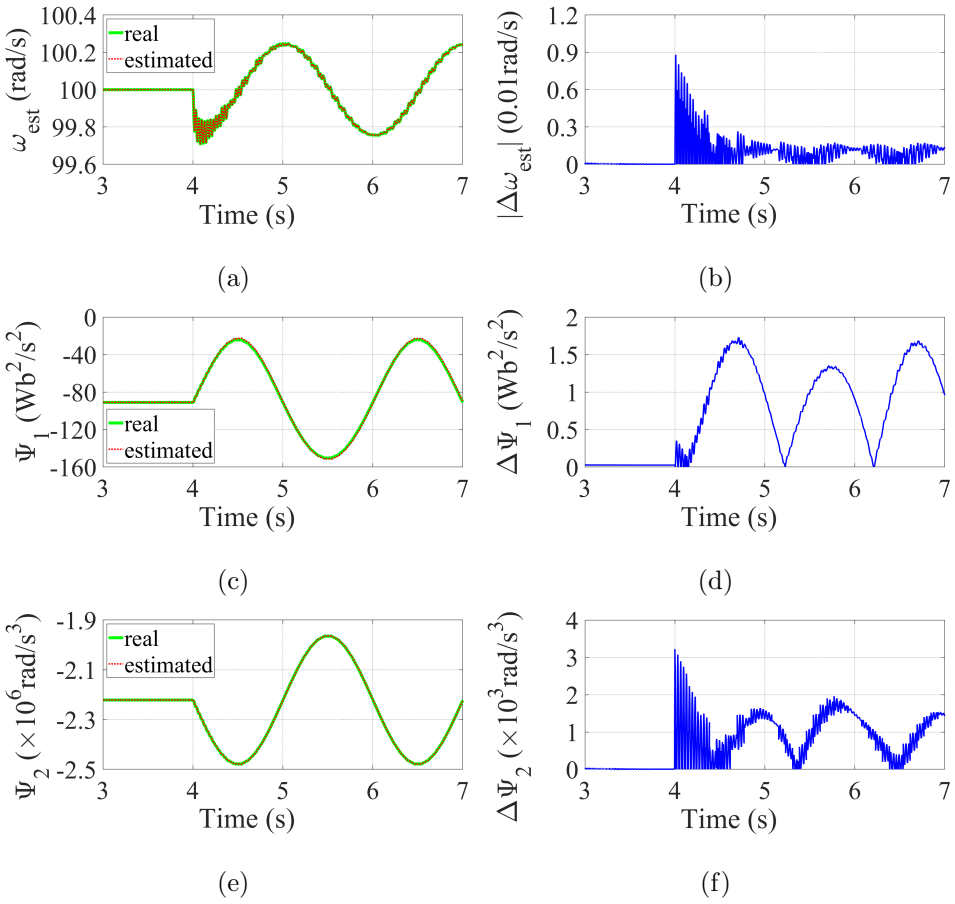

Figure 8: Estimation performance of the CSPO under time-varying load torque disturbance.

provide power to both the motor and PE board in different voltage level, and a DS1104 dSPACE controller with breakout box. In the motor bench, the target IM is coupled with a DC motor that produces the expected load torque. In the practical implementation, the first-order Euler discretization method is used for compiling the simulation model into C programming code in the dSPACE DS1104 controller board, whose CPU clock is 250 MHz. Considering both the sampling rate and computational capability of the controller hardware, the sampling time adopted for practical implementation is

Table 3: Simulation performance indices and reductions of VC plus MRAS and SSNAC

Indices \ Method		VC+MRAS	SSNAC	Reduc.
Case 1	Max. Flux Error	6.9%	0.13%	98.1%
	Flux IAE ($\times 10^{-3}$)	8.2	0.1	99%
	Max. Speed Error	7.8%	1.6%	79.5%
	Speed IAE	20.4	3.8	81%
Case 2	Max. Flux Error	3.7%	0.052%	99%
	Flux IAE ($\times 10^{-3}$)	3.0	0.0042	99%
	Max. Speed Error	2.2%	0.29%	87%
	Speed IAE	6.3	0.77	88%

set to 0.0001 s. The observer and controller are operating under the same implementation environment and sampling time. Thus, the whole control system with proposed algorithm takes less than 25,000 computational clock cycles in total. If the proposed algorithm is implemented in a computational unit with lower clock frequency, the sampling time should be increased correspondingly to allow the computational unit to have enough time to run out the algorithm. In the experiment, the nominal value of motor parameters has been used. The unmeasured parameter varying during operations is considered as the uncertainty and external disturbance.

6.2. Speed tracking under constant load disturbance

The control parameters of experiments are the same with that in simulation. The load torque disturbance and the speed references use the same profiles as in simulation, as shown in Figure 10(a) and 10(b). In the hardware implementation, the speed estimation performance and its estimation error are given in Figure 10(c) and 10(d). From the speed estimation result,

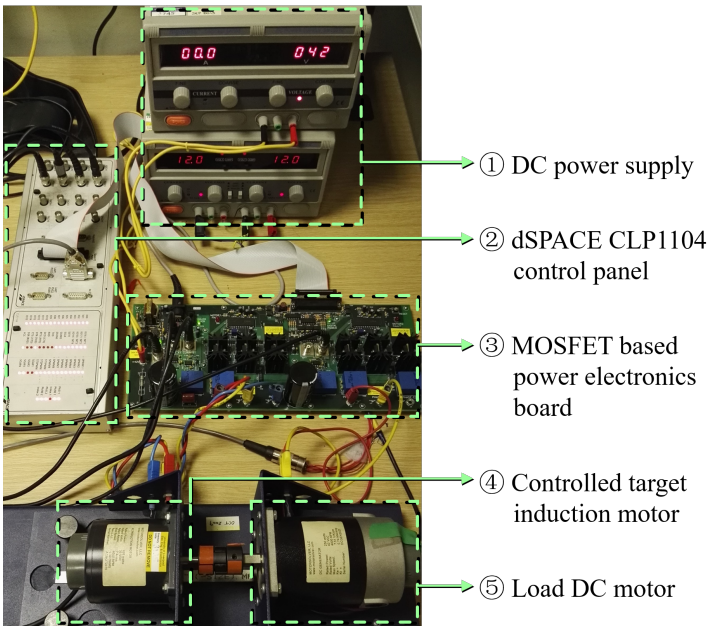

Figure 9: Experimental setup of IM speed sensorless control.

the maximum speed estimation error are around 2 rad/s during speed rising and less than 0.7 rad/s in steady state. As the real perturbation of the IM system is difficult to be obtained in experimental test, the performance of perturbation estimation cannot be given.

In the rotor flux and speed tracking, the rotor flux is controlled to stay at 0.0265 Wb while rotor speed increases from 0 to 80 rad/s and stays at this speed. Their performance is shown in Figure 11(a) and 11(b). During the period of speed rising, the flux and speed tracking error of VC plus MRAS can reach 18.2% and 8.6rad/s, respectively. As shown in Figure 11(c) and 11(d), the SSNAC can reduce the flux regulation error to 13.2% and speed tracking error to 3.1 rad/s. More than half of the speed tracking error has been reduced.

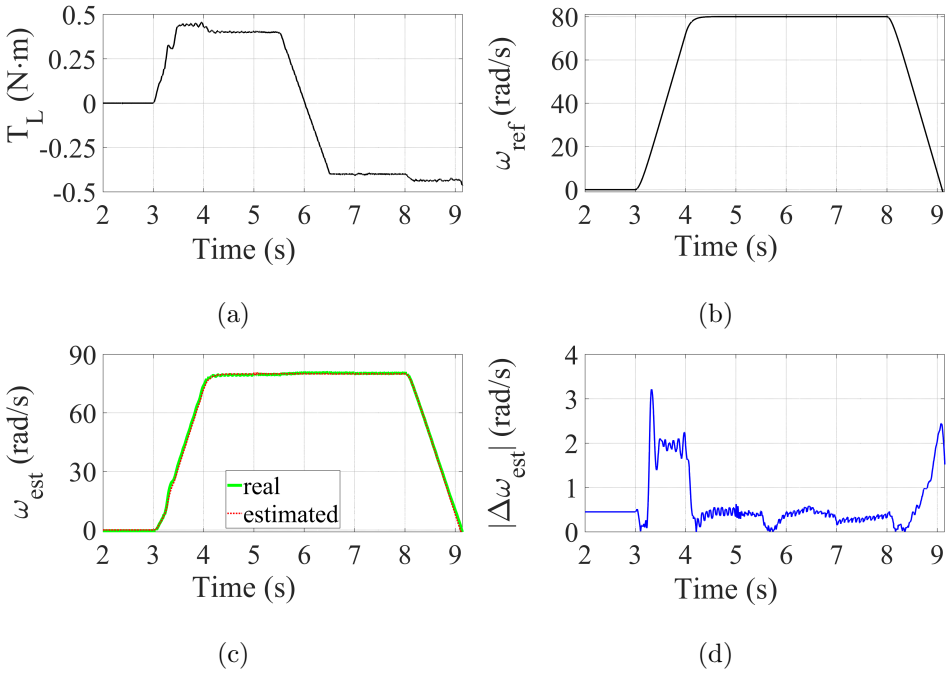

Figure 10: Experimental results of speed tracking under constant load disturbance. (a) Load disturbance, (b) speed reference, (c) speed estimation, (d) estimation error.

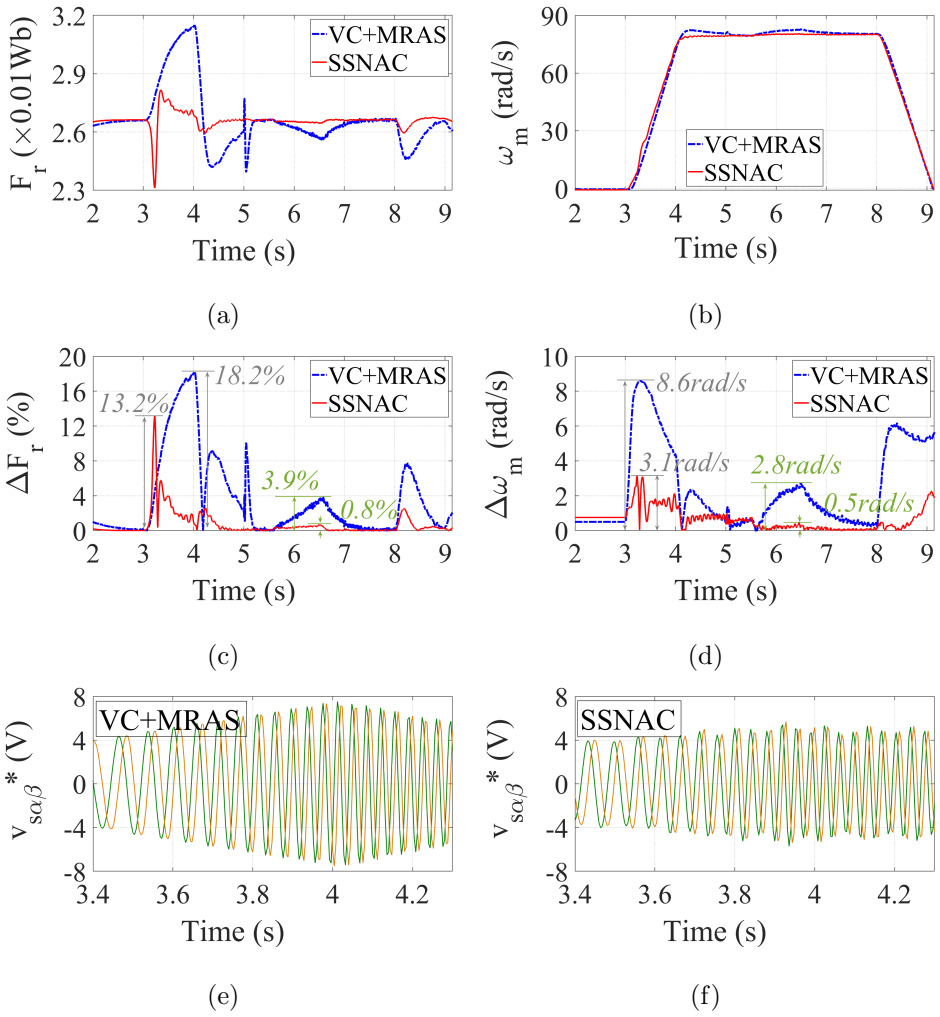

Figure 11: Experimental results of speed tracking under constant load disturbance. (a) rotor flux performance, (b) rotor speed performance, (c) flux error, (d) speed error, (e) stator voltage control input of VC plus MRAS, and (f) stator voltage control input of SSNAC.

In addition, after the rotor speed reaches the steady state, the change of load torque disturbance from positive 0.4 Nm to negative 0.4 Nm causes the speed varying at t=6 s. The regulation performance of flux and speed under the change of load torque using VC plus MRAS method is about 3.9% and 2.8 rad/s, respectively. While the SSNAC reduces the flux regulation error to 0.8% and speed tracking error to 0.5 rad/s. It verifies that the SSNAC has obvious improvement in the sensorless tracking of both flux and rotor speed. Figure 11(e) and 11(f) show the control inputs of stator voltage of VC plus MRAS and SSNAC. From which it can be found that the SSNAC has less voltage input in average and its peak value is less than 6V while that of VC plus MRAS is close to 8 V.

The numerical comparison of performance indices are summarised in Table 4 case 1. The results show that, in speed tracking under constant load torque, the SSNAC performs better than that of VC plus MRAS method with the reduction of maximum and IAE of flux regulation error by 21% and 77%, respectively. And the reduction of that on speed tracking error by 33% and 75%. The reduction of SSNAC in experiments is less than that in simulation. The reason of that is caused by the uncertainty of IM parameters in rotor-flux model. In experiments, the effective parameters of IM system can be varying with ambient temperature and the delay of current feedback from transducers, which is assumed ideal in simulation test. In order to compare the reduction of flux and speed tracking error in an obvious way, the bar chart of performance indices is given for this case in Figure 14(a).

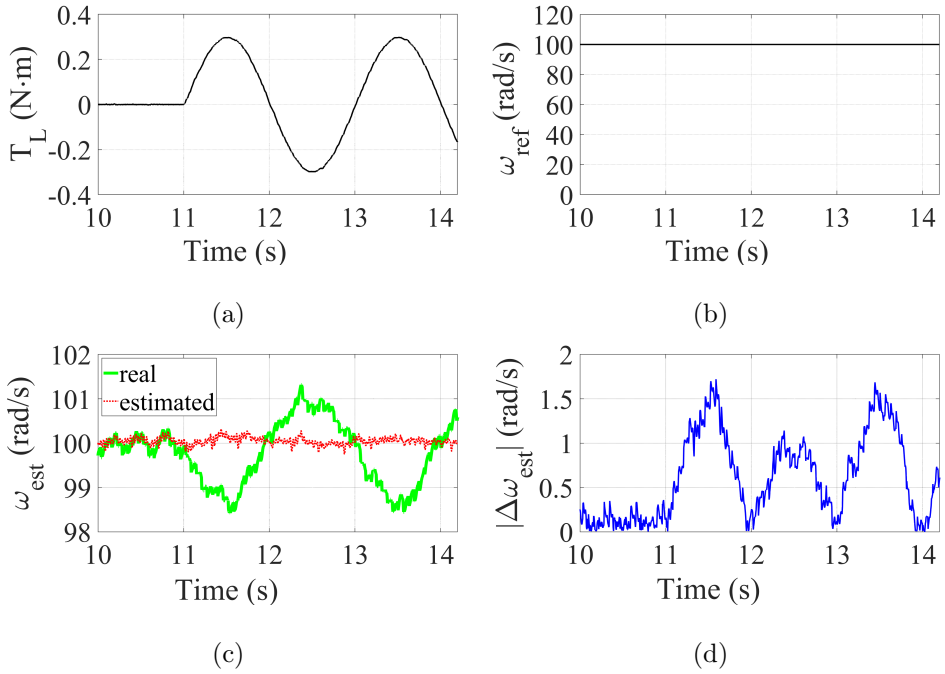

Figure 12: Experimental results of constant speed regulation under time-varying load torque disturbance. (a) Load disturbance, (b) speed reference, (c) speed estimation, (d) estimation error.

6.3. Time-varying load torque disturbance test

In constant speed regulation, the IM rotor speed is expected to be maintained at 100 rad/s, as in Figure 12(b). A sinewave shape time varying load torque disturbance is then applied to the IM as shown in Figure 12(a). Under this case, the rotor speed estimation performance of the CSPO is shown in Figure 12(c) and its estimation error is shown in Figure 12(d). The result shows that the designed observer can estimate the rotor speed of the target IM system under time-varying load torque disturbance with its estimation error less than 1.7% in any time and 0.8% in average.

The flux and speed regulation performance and their relative regulation error are shown in Figure 13(a) and 13(b) and their relative regulation error

Table 4: Experiment performance indices and reductions of VC plus MRAS and SSNAC

	Indices \ Method	VC+MRAS	SSNAC	Reduc.
Case 1	Maximum Flux Error	18.3%	13%	21%
	Flux IAE ($\times 10^{-3}$)	9.3	2.1	77%
	Maximum Speed Error	4.2%	2.8%	33%
	Speed IAE	31.0	7.7	75%
Case 2	Maximum Flux Error	3.7%	0.78%	79%
	Flux IAE ($\times 10^{-3}$)	2.3	0.46	80%
	Maximum Speed Error	3.2%	1.6%	52%
	Speed IAE	8.9	6.4	28%

are shown in Figure 13(c) and 13(d). The peak regulation error of flux and speed in VC plus MRAS method are 3.7% and 3.2%, while that of the SSNAC are reduced to 0.8% and 1.6%. The control input of SSNAC does not have any increment to achieve the improvement of control performance in flux and speed regulation as shown in Figure 13(e) and 13(f)

The performance indices are summarised and compared between SSNAC and traditional VC plus MRAS method in Table 4 case 2 and Figure 14(b). The results show that the SSNAC reduced the flux regulation error and its IAE by 79% and 80% while the reduction of rotor speed regulation error is 52% in peak and 28% in IAE. The effectiveness of the speed sensorless control using SSNAC to fully decouple the interaction of flux and rotor speed has been verified with obvious better performance.

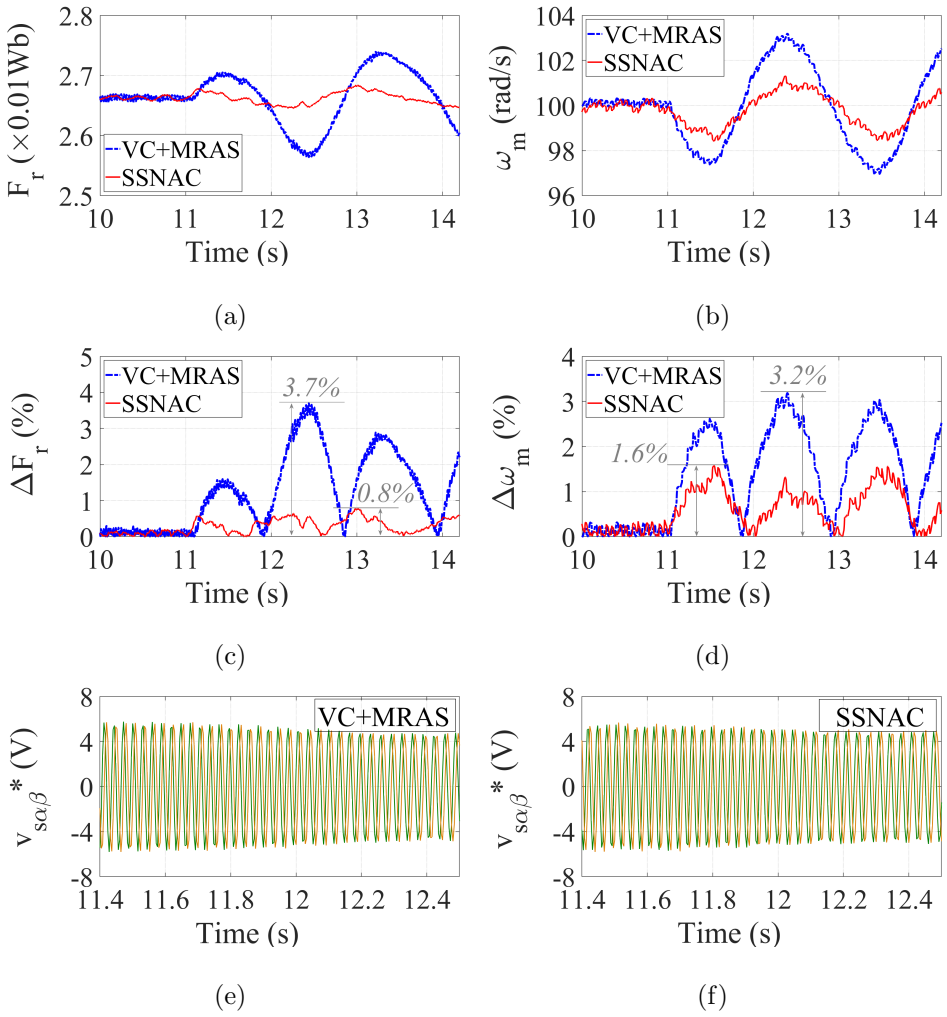

Figure 13: Experimental results of constant speed regulation under time-varying load torque disturbance. (a) rotor flux performance, (b) rotor speed performance, (c) flux error, (d) speed error, (e) stator voltage control input of VC plus MRAS, and (f) stator voltage control input of SSNAC.

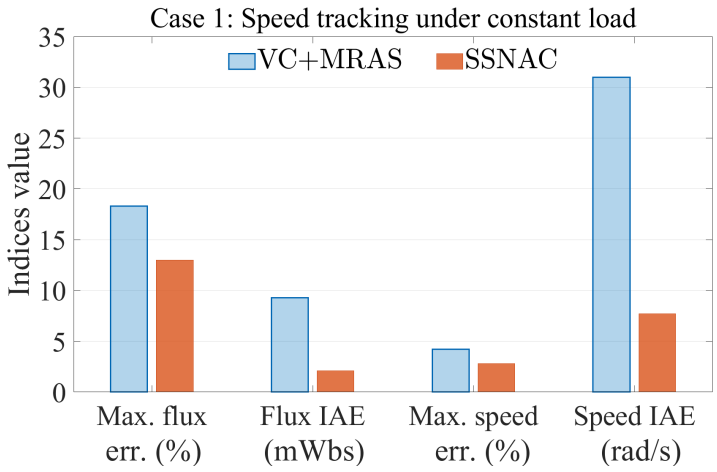

(a)

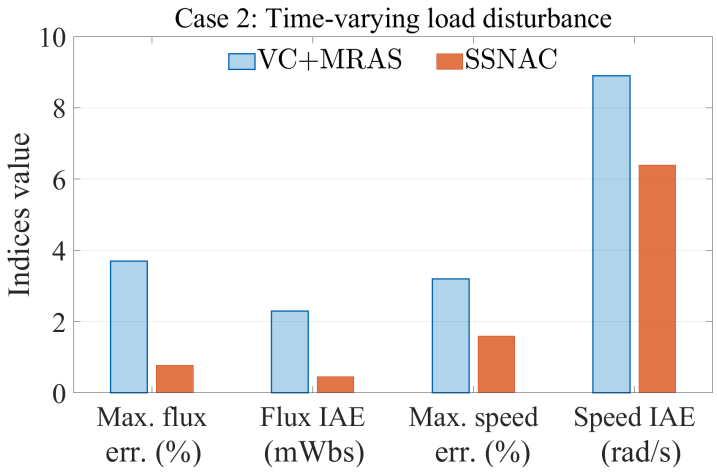

(b)

Figure 14: Comparison of performance indices of experimental results in (a) speed tracking under constant load disturbance, (b) constant speed regulation under time-varying load disturbance.

7. Conclusion

This paper proposed a speed sensorless nonlinear adaptive control to achieve the fully decoupling control of the flux and speed of IM without the usage of speed sensor. The proposed nonlinear adaptive controller has been used together with the traditional rotor-flux MRAS speed estimator. Then a combined speed and perturbation observer (CSPO) is designed to estimate the rotor speed and its perturbation term simultaneously. The estimated speed is used as feedback in the speed loop and the estimated lumped perturbation terms is used to compensate the real perturbation that contains the nonlinear dynamics, external load disturbance and parameter uncertainties. Moreover, the CSPO replaced the PI regulator in the MRAS speed observer and thus reduced the complexity of SSNAC controller. With the estimated speed and perturbation terms from the CSPO, the IM system can be fully decoupled and controlled without speed sensor. The stability of SSNAC with CSPO has been proved using Lyapunov theory. The effectiveness of SSNAC has been verified in both simulation and experiment studies. The results show that the SSNAC performs better in speed tracking and under unknown load disturbance without speed sensors comparing with traditional VC plus MRAS method. It validated that the estimation of speed and its perturbation term using the CSPO can provide speed sensorless control as well as the fully decoupling of interactions in the nonlinear IM system.

In summary, the main advantages of the proposed control approach are given as below:

- The proposed control approach integrates nonlinear control technology and speed estimation technology, so it not only reduces the use of PI

regulator in the traditional MRAS speed estimator, but also enables overall stability analysis.

- The proposed control method can estimate the rotor speed and its disturbance term simultaneously, thus, it reduces the dependence of speed sensors, accurate models and parameters to improve the robustness of the control system.

- The proposed control approach can perform much better speed tracking performance under model uncertainty and unknown load disturbance.

The limitations of this work are listed as follows. First, the proposed approach requires a high-gain observer in the SPO design. Therefore, when speed estimation and perturbation estimation are combined, the selection of the optimal gains becomes difficult. The best way to adjust the observer gain will be considered in future studies. Secondly, the speed sensorless technology in this article uses the MRAS method, which requires accurate models and parameters. Although the perturbation estimation approach reduces the dependency of accurate model and parameters, more other speed estimation methods will be studied in the future to choose the most robust way to combine the speed sensorless techniques with the perturbation estimation approach.

In future work, the authors will study the method of finding the optimal gains for the observer and the controller in both theoretical and practical aspects. And compare the combination of different types of speed sensorless methods and perturbation estimation-based control methods under different conditions and application scenarios. In addition, the authors will continue

to study the sensitivity of this method to system parameter uncertainty and fault detection methods in hardware implementation.

Appendix A. Proof of $a_2 > 0$

Since the $\psi_{r\alpha}$ and $\psi_{r\beta}$ are in stationary frame, assuming that the angle of rotor flux is θ_r. Then it can be represented as $\psi_{r\alpha} = |\psi_r| \sin\theta_r$ and $\psi_{r\beta} = |\psi_r| \cos\theta_r$. Then assuming that the estimation error of rotor flux angle is $\widetilde{\theta}_r$, and one can get $\hat{\psi}_{r\alpha} = \left|\hat{\psi}_r\right| \sin\left(\theta_r + \widetilde{\theta}_r\right)$ and $\hat{\psi}_{r\beta} = \left|\hat{\psi}_r\right| \cos\left(\theta_r + \widetilde{\theta}_r\right)$. On the basis of these, it can be proved that

$$\begin{aligned}
\frac{a_2}{P} &= \psi_{r\alpha}\hat{\psi}_{r\alpha} + \psi_{r\beta}\hat{\psi}_{r\beta} \qquad \text{(A.1)} \\
&= |\psi_r| \sin\theta_r \cdot \left|\hat{\psi}_r\right| \sin\left(\theta_r + \widetilde{\theta}_r\right) + |\psi_r| \cos\theta_r \cdot \left|\hat{\psi}_r\right| \cos\left(\theta_r + \widetilde{\theta}_r\right) \\
&= |\psi_r| \left|\hat{\psi}_r\right| \cdot \sin\theta_r \cdot \sin\left(\theta_r + \widetilde{\theta}_r\right) + |\psi_r| \left|\hat{\psi}_r\right| \cdot \cos\theta_r \cdot \cos\left(\theta_r + \widetilde{\theta}_r\right) \\
&= |\psi_r| \left|\hat{\psi}_r\right| \left(\sin^2\theta_r \cos\widetilde{\theta}_r + \cos^2\theta_r \cos\widetilde{\theta}_r\right) \\
&= |\psi_r| \left|\hat{\psi}_r\right| \cos\widetilde{\theta}_r
\end{aligned}$$

Thus, if $\left|\widetilde{\theta}_r\right| < 90°$, a_2 can be proved as a positive value. In normal condition of IM control, the estimation error of rotor angle will be far less than 90 degree. Thus, in this paper, it assumes that $a_2 > 0$ in all conditions.

Appendix B. Proof of λ is bounded

From equation (35), since $a_2\omega_m$ and a_3 are calculated from the physical variables, they can be assumed as bounded based on the fact that the target system is a physical system containing mechanical and electrical processes, and its variables will be within a suitable range instead of infinite values.

Thus, this section will only prove the boundness of $k_{\mathrm{I}} \int \epsilon \, dt$. From (20), ϵ can be rewritten as

$$\begin{aligned}
\epsilon &= \psi_{\mathrm{r}\beta}\hat{\psi}_{\mathrm{r}\alpha} - \psi_{\mathrm{r}\alpha}\hat{\psi}_{\mathrm{r}\beta} \\
&= \left|\hat{\psi}_{\mathrm{r}}\right| \sin\left(\theta_{\mathrm{r}} + \widetilde{\theta}_{\mathrm{r}}\right) \cdot |\psi_{\mathrm{r}}| \cos\theta_{\mathrm{r}} - \left|\hat{\psi}_{\mathrm{r}}\right| \cos\left(\theta_{\mathrm{r}} + \widetilde{\theta}_{\mathrm{r}}\right) \cdot |\psi_{\mathrm{r}}| \sin\theta_{\mathrm{r}} \\
&= \left|\hat{\psi}_{\mathrm{r}}\right| |\psi_{\mathrm{r}}| \cdot \left(\cos\theta_{\mathrm{r}} \cdot \sin\left(\theta_{\mathrm{r}} + \widetilde{\theta}_{\mathrm{r}}\right) - \sin\theta_{\mathrm{r}} \cdot \cos\left(\theta_{\mathrm{r}} + \widetilde{\theta}_{\mathrm{r}}\right)\right) \\
&= \left|\hat{\psi}_{\mathrm{r}}\right| |\psi_{\mathrm{r}}| \sin\widetilde{\theta}_{\mathrm{r}}
\end{aligned} \tag{B.1}$$

Then it is easy to find that

$$\int \epsilon \, dt = \left|\hat{\psi}_{\mathrm{r}}\right| |\psi_{\mathrm{r}}| \cos\widetilde{\theta}_{\mathrm{r}} \leq \left|\hat{\psi}_{\mathrm{r}}\right| |\psi_{\mathrm{r}}| \tag{B.2}$$

Thus $\int \epsilon \, dt$ is proved as bounded since the rotor flux ψ_r has the upper limit according to the design and manufacturing. And on the basis of this, λ can be proved as bounded then.

References

Bhowate, A., Aware, M., Sharma, S., 2019. Predictive torque control with online weighting factor computation technique to improve performance of induction motor drive in low speed region. IEEE Access 7, 42309–42321. doi:10.1109/ACCESS.2019.2908289.

Bimal, K., 2002. Bose. Modern power electronics and AC drives .

Boukas, T., Habetler, T., 2004. High-performance induction motor speed control using exact feedback linearization with state and state derivative feedback. IEEE Transactions on Power Electronics 19, 1022–1028. doi:10.1109/TPEL.2004.830042.

Callegaro, A.D., Nalakath, S., Srivatchan, L.N., Luedtke, D., Preindl, M., 2018. Optimization-based position sensorless control for induction machines, in: 2018 IEEE Transportation Electrification Conference and Expo (ITEC), IEEE. pp. 460–466. doi:10.1109/ITEC.2018.8450137.

Chen, J., Jiang, L., Yao, W., Wu, Q., 2014. Perturbation estimation based nonlinear adaptive control of a full-rated converter wind turbine for fault ride-through capability enhancement. IEEE Transactions on Power Systems, 29, 2733–2743. doi:10.1109/TPWRS.2014.2313813.

Chen, J., Yao, W., Ren, Y., Wang, R., Zhang, L., Jiang, L., 2019a. Nonlinear adaptive speed control of a permanent magnet synchronous motor: A perturbation estimation approach. Control Engineering Practice 85, 163–175. doi:10.1016/j.conengprac.2019.01.019.

Chen, J., Yao, W., Zhang, C.K., Ren, Y., Jiang, L., 2019b. Design of robust MPPT controller for grid-connected PMSG-based wind turbine via perturbation observation based nonlinear adaptive control. Renewable Energy 134, 478–495. doi:10.1016/j.renene.2018.11.048.

Costa, B.L.G., Graciola, C.L., Angélico, B.A., Goedtel, A., Castoldi, M.F., de Andrade Pereira, W.C., 2019. A practical framework for tuning DTC-SVM drive of three-phase induction motors. Control Engineering Practice 88, 119–127.

Ellis, G., 2002. Observers in control systems: a practical guide. Elsevier.

Englert, T., Graichen, K., 2020. Nonlinear model predictive torque con-

trol and setpoint computation of induction machines for high performance applications. Control Engineering Practice 99, 104415.

Feng, G., Liu, Y.F., Huang, L., 2004. A new robust algorithm to improve the dynamic performance on the speed control of induction motor drive. IEEE Transactions on Power Electronics 19, 1614–1627. doi:10.1109/TPEL.2004.836619.

Finch, J., Giaouris, D., 2008. Controlled ac electrical drives. IEEE Transactions on Industrial Electronics, 55, 481–491. doi:10.1109/TIE.2007.911209.

Gadoue, S., Giaouris, D., Finch, J., 2010. MRAS sensorless vector control of an induction motor using new sliding-mode and fuzzy-logic adaptation mechanisms. IEEE Transactions on Energy Conversion, 25, 394–402. doi:10.1109/TEC.2009.2036445.

Grabowski, P., Kazmierkowski, M., Bose, B., Blaabjerg, F., 2000. A simple direct-torque neuro-fuzzy control of PWM-inverter-fed induction motor drive. IEEE Transactions on Industrial Electronics, 47, 863–870. doi:10.1109/41.857966.

Guzinski, J., Abu-Rub, H., 2013. Speed sensorless induction motor drive with predictive current controller. IEEE Transactions on Industrial Electronics 60, 699–709. doi:10.1109/TIE.2012.2205359.

Habibullah, M., Lu, D.D.C., 2015. A speed-sensorless FS-PTC of induction motors using extended kalman filters. IEEE Transactions on Industrial Electronics 62, 6765–6778. doi:10.1109/TIE.2015.2442525.

Han, J., 2009. From PID to active disturbance rejection control. IEEE Transactions on Industrial Electronics, 56, 900–906. doi:10.1109/TIE.2008.2011621.

Holakooie, M.H., Ojaghi, M., Taheri, A., 2019. Modified DTC of a six-phase induction motor with a second-order sliding-mode MRAS-based speed estimator. IEEE Transactions on Power Electronics 34, 600–611. doi:10.1109/TPEL.2018.2825227.

Holtz, J., 2005. Sensorless control of induction machines- with or without signal injection? IEEE Transactions on Industrial Electronics, 53, 7–30. doi:10.1109/TIE.2005.862324.

Hu, Y., Song, X., Cao, W., Ji, B., 2014. New SR drive with integrated charging capacity for plug-in hybrid electric vehicles (PHEVs). IEEE Transactions on Industrial Electronics 61, 5722–5731. doi:10.1109/TIE.2014.2304699.

Jiang, L., Wu, Q., Wen, J., 2004. Decentralized nonlinear adaptive control for multimachine power systems via high-gain perturbation observer. IEEE Transactions on Circuits and Systems I: Regular Papers, 51, 2052–2059. doi:10.1109/TCSI.2004.835657.

Jiang, L., Wu, Q.H., 2002. Nonlinear adaptive control via sliding-mode state and perturbation observer. IEE Proceedings - Control Theory and Applications 149, 269–277. doi:10.1049/ip-cta:20020470.

Kivanc, O.C., Ozturk, S.B., 2018. Sensorless PMSM drive based on stator feedforward voltage estimation improved with MRAS multi-

parameter estimation. IEEE/ASME Transactions on Mechatronics doi:10.1109/TMECH.2018.2817246.

Li, J., Ren, H.P., ru Zhong, Y., 2015. Robust speed control of induction motor drives using first-order auto-disturbance rejection controllers. IEEE Transactions on Industry Applications 51, 712–720. doi:10.1109/TIA.2014.2330062.

Li, J., Xu, L., Zhang, Z., 2005. An adaptive sliding-mode observer for induction motor sensorless speed control. IEEE Transactions on Industry Applications 41, 1039–1046. doi:10.1109/ICEMS.2019.8922535.

Li, S., Xia, C., Zhou, X., 2012. Disturbance rejection control method for permanent magnet synchronous motor speed-regulation system. Mechatronics 22, 706–714. doi:10.1016/j.mechatronics.2012.02.007.

Liu, Y., Zhao, J., Wang, R., Huang, C., 2013. Performance improvement of induction motor current controllers in field-weakening region for electric vehicles. IEEE Transactions on Power Electronics 28, 2468–2482. doi:10.1109/TPEL.2012.2217757.

Marchesoni, M., Passalacqua, M., Vaccaro, L., Calvini, M., Venturini, M., 2020. Performance improvement in a sensorless surface-mounted PMSM drive based on rotor flux observer. Control Engineering Practice 96, 104276.

Marino, R., Peresada, S., Valigi, P., 1993. Adaptive input-output linearizing control of induction motors. IEEE Transactions on Automatic Control 38, 208–221. doi:10.1109/9.250510.

Marino, R., Tomei, P., Verrelli, C., 2005. Adaptive control for speed-sensorless induction motors with uncertain load torque and rotor resistance. International Journal of Adaptive Control and Signal Processing 19, 661–685. doi:10.1002/acs.874.

Marino, R., Tomei, P., Verrelli, C.M., 2008. An adaptive tracking control from current measurements for induction motors with uncertain load torque and rotor resistance. Automatica 44, 2593–2599. doi:10.1016/j.automatica.2008.02.023.

Nasiri, A., 2007. Full digital current control of permanent magnet synchronous motors for vehicular applications. IEEE Transactions on Vehicular Technology 56, 1531–1537. doi:10.1109/TVT.2007.896969.

Ohyama, K., Asher, G., Sumner, M., 2005. Comparative analysis of experimental performance and stability of sensorless induction motor drives. IEEE Transactions on Industrial Electronics 53, 178–186. doi:10.1109/TIE.2005.862298.

Perin, M., Pereira, L.A., Pereira, L.F., Sogari, P.A., Nicol, G., 2021. A method to estimate parameters of five-phase induction machines including the third-harmonic airgap field. Control Engineering Practice 111, 104792.

Proca, A., Keyhani, A., 2007. Sliding-mode flux observer with online rotor parameter estimation for induction motors. IEEE Transactions on Industrial Electronics, 54, 716–723. doi:10.1109/TIE.2007.891786.

Pyrkin, A., Bobtsov, A., Vedyakov, A., Ortega, R., Vediakova, A., Sinetova, M., 2019. DREM-based adaptive observer for induction motors, in: 2019

IEEE 58th Conference on Decision and Control (CDC), IEEE. pp. 648–653. doi:10.1109/CDC40024.2019.9029739.

Ravi Teja, A., Chakraborty, C., Maiti, S., Hori, Y., 2012. A new model reference adaptive controller for four quadrant vector controlled induction motor drives. IEEE Transactions on Industrial Electronics, 59, 3757–3767. doi:10.1109/TIE.2011.2164769.

Rehman, H., Xu, L., 2011. Alternative energy vehicles drive system: Control, flux and torque estimation, and efficiency optimization. IEEE Transactions on Vehicular Technology, 60, 3625–3634. doi:10.1109/TVT.2011.2163537.

Ren, Y., Li, L., Brindley, J., Jiang, L., 2016. Nonlinear PI control for variable pitch wind turbine. Control Engineering Practice 50, 84–94. doi:10.1016/j.conengprac.2016.02.004.

Rind, S.J., Ren, Y., Hu, Y., Wang, J., Jiang, L., 2017. Configurations and control of traction motors for electric vehicles: A review. Chinese Journal of Electrical Engineering 3, 1–17. doi:10.23919/CJEE.2017.8250419.

Schauder, C., 1992. Adaptive speed identification for vector control of induction motors without rotational transducers. IEEE Transactions on Industry Applications 28, 1054–1061. doi:10.1109/28.158829.

Suetake, M., da Silva, I.N., Goedtel, A., 2011. Embedded DSP-based compact fuzzy system and its application for induction-motor V/f speed control. IEEE Transactions on Industrial Electronics 58, 750–760. doi:10.1109/TIE.2010.2047822.

Sun, X., Chen, L., Yang, Z., Zhu, H., 2013. Speed-sensorless vector control of a bearingless induction motor with artificial neural network inverse speed observer. IEEE/ASME Transactions on mechatronics 18, 1357–1366. doi:10.1109/TMECH.2012.2202123.

Sung, W., Shin, J., Jeong, Y.s., 2012. Energy-efficient and robust control for high-performance induction motor drive with an application in electric vehicles. IEEE transactions on vehicular technology 61, 3394–3405. doi:10.1109/TVT.2012.2213283.

Tarchała, G., Orłowska-Kowalska, T., 2018. Equivalent-signal-based sliding mode speed MRAS-type estimator for induction motor drive stable in the regenerating mode. IEEE Transactions on Industrial Electronics 65, 6936–6947. doi:10.1109/TIE.2018.2795518.

Tilli, A., Conficoni, C., 2016. Semiglobal uniform asymptotic stability of an easy-to-implement PLL-like sensorless observer for induction motors. IEEE Transactions on Automatic Control 61, 3612–3618. doi:10.1109/TAC.2016.2521728.

Verrelli, C.M., Lorenzani, E., Fornari, R., Mengoni, M., Zarri, L., 2018. Steady-state speed sensor fault detection in induction motors with uncertain parameters: A matter of algebraic equations. Control Engineering Practice 80, 125–137.

Wang, H., Liu, Y.c., Ge, X., 2018a. Sliding-mode observer-based speed-sensorless vector control of linear induction motor with a parallel secondary

resistance online identification. IET Electric Power Applications 12, 1215–1224. doi:10.1049/iet-epa.2018.0049.

Wang, Y., Zhou, L., Bortoff, S.A., Satake, A., Furutani, S., 2018b. An approximate high gain observer for speed-sensorless estimation of induction motors. IEEE/CAA Journal of Automatica Sinica doi:10.1109/TMECH.2012.2202123.

Wu, L., Zheng, W.X., Gao, H., 2013. Dissipativity-based sliding mode control of switched stochastic systems. IEEE Transactions on Automatic Control 58, 785–791. doi:10.1109/TAC.2012.2211456.

Yang, S., Ding, D., Li, X., Xie, Z., Zhang, X., Chang, L., 2018. A decoupling estimation scheme for rotor resistance and mutual inductance in indirect vector controlled induction motor drives. IEEE Transactions on Energy Conversion doi:10.1109/TEC.2018.2880796.

Yoo, D., Yau, S.T., Gao, Z., 2007. Optimal fast tracking observer bandwidth of the linear extended state observer. International Journal of Control 80, 102–111. doi:10.1080/00207170600936555.

Zaky, M.S., Metwaly, M.K., Azazi, H.Z., Deraz, S.A., 2018. A new adaptive SMO for speed estimation of sensorless induction motor drives at zero and very low frequencies. IEEE Transactions on Industrial Electronics 65, 6901–6911. doi:10.1109/TIE.2018.2793206.

Zhang, X., 2013. Sensorless induction motor drive using indirect vector controller and sliding-mode observer for electric vehicles. IEEE Transactions on Vehicular Technology 62, 3010–3018. doi:10.1109/TVT.2013.2251921.